GLIA

WILEY

RESEARCH ARTICLE

Amyloid-β plaques affect astrocyte Kir4.1 protein expression but not function in the dentate gyrus of APP/PS1 mice

Christiaan F. M. Huffels[1] | Lana M. Osborn[2] | Lianne A. Hulshof[1] |
Lieneke Kooijman[2] | Lukas Henning[3] | Christian Steinhäuser[3] | Elly M. Hol[1]

[1]Department of Translational Neuroscience, University Medical Center Utrecht Brain Center, Utrecht University, Utrecht, The Netherlands

[2]Swammerdam Institute for Life Sciences, Center for Neuroscience, University of Amsterdam, Amsterdam, The Netherlands

[3]Institute of Cellular Neurosciences, Medical Faculty, University of Bonn, Bonn, Germany

Correspondence
Elly M. Hol, Department of Translational Neuroscience, University Medical Center Utrecht Brain Center, Utrecht University, Utrecht, The Netherlands.
Email: e.m.hol-2@umcutrecht.nl

Abstract

Alzheimer pathology is accompanied by astrogliosis. Reactive astrocytes surrounding amyloid plaques may directly affect neuronal communication, and one of the mechanisms by which astrocytes impact neuronal function is by affecting K^+ homeostasis. Here we studied, using hippocampal slices from 9-month-old Alzheimer mice (APP/PS1) and wild-type littermates, whether astrocyte function is changed by analyzing Kir4.1 expression and function and astrocyte coupling in astrocytes surrounding amyloid-β plaques. Immunohistochemical analysis of Kir4.1 protein in the dentate gyrus revealed localized increases in astrocytes surrounding amyloid-β plaque deposits. We subsequently focused on changes in astrocyte function by using patch-clamp slice electrophysiology on both plaque- and non-plaque associated astrocytes to characterize general membrane properties. We found that Ba^{2+}-sensitive Kir4.1 conductance in astrocytes surrounding plaques was not affected by changes in Kir4.1 protein expression. Additional analysis of astrocyte gap junction coupling efficiency in the dentate gyrus revealed no apparent changes. Quantification of basic features of glutamatergic transmission to granule cells did not indicate disturbed neuronal communication in the dentate gyrus of APP/PS1 mice. Together, these results suggest that astrocytes in the dentate gyrus of APP/PS1 mice maintain their ability to buffer extracellular K^+ and attempt to rectify imbalances in K^+ concentration to maintain normal neuronal and synaptic function, possibly by localized increases in Kir4.1 protein expression. Our earlier transcriptomic data indicated that chronically activated astrocytes lose their neuronal support function. Here we show that, despite localized increased Kir4.1 protein expression, astrocyte Kir4.1 channel dysfunction is likely not involved in the pathogenesis of Alzheimer's disease.

KEYWORDS
Alzheimer's disease, astrocytes, amyloid-β plaques, dentate gyrus, glia, inward rectification, potassium channels, reactive gliosis, RRID:AB_10013382, RRID:AB_2040120, RRID: AB_2651133, RRID:AB_477010, RRID:AB_570666, RRID:AB_662807

Christiaan F. M. Huffels and Lana M. Osborn contributed equally to this work.

1 | INTRODUCTION

Alzheimer's disease (AD) is the main form of dementia in the elderly and yet the exact mechanisms underlying its pathology remain unknown (Querfurth & LaFerla, 2010). A common hallmark of AD, along with neurofibrillary tangles and amyloid-β (Aβ) plaques, is the presence of reactive astrocytes (Kamphuis et al., 2012, 2014; Pekny et al., 2016). Classically, astrogliosis is characterized by morphological changes of astrocytes and an increase in the expression of the intermediate filament protein glial fibrillary acidic protein (GFAP) (Escartin et al., 2021; Pekny et al., 2016). Although aberrant function and protein expression of reactive astrocytes in AD have been studied extensively, its exact physiological consequences are still under debate. Given the intimate relationship astrocytes have with neurons (e.g., recycling neurotransmitters, regulating energy metabolism and maintaining K^+ homeostasis), changes in astrocyte function and protein expression are likely a critical component in the progression of the cognitive decline present in AD (Osborn et al., 2016).

Both AD patient and mouse model data reveal that astrocytes alter their molecular phenotype in response to AD pathology (Bossers et al., 2010; Orre, Kamphuis, Osborn, Jansen, et al., 2014; Sekar et al., 2015). Indeed, transcriptomic analysis shows that with disease progression astrocytes shift towards an immune signaling phenotype, while genes involved in the neuronal support function become down regulated (Orre, Kamphuis, Osborn, Melief, et al., 2014). Functional phenotypic changes in reactive astrocytes have been reported and include reduced glutamate transporter expression (Jacob et al., 2007; Malm et al., 2007; Schallier et al., 2011), impaired insulin signaling (Meeker et al., 2015; Moloney et al., 2010), increased responsiveness to AMPA/kainate receptor signaling and changes in gap junction coupling efficiency (Peters et al., 2009). Additionally, reactive astrocytes have been shown to promote over-activation of neuronal networks (Ortinski et al., 2010), an increase in astrocyte Ca^{2+} signaling (Delekate et al., 2014; Kuchibhotla et al., 2009), as well as an increase in GABA release from reactive astrocytes (Jo et al., 2014; Wu et al., 2014). Moreover, since astrocytes play an essential role in maintaining ion homeostasis (Rose & Verkhratsky, 2016), including the buffering of extracellular K^+ (Steinhäuser et al., 2012), K^+ and Na^+ ion imbalances are present in tissue from AD patients and primary astrocyte cultures exposed to Aβ (Vitvitsky et al., 2012).

For astrocytes to effectively carry out their function in maintaining ion homeostasis, their plasma membrane is characterized by a high K^+ conductance, entailing a very negative resting membrane potential close to the K^+ equilibrium potential. In addition, astrocytes are electrically coupled to neighboring astrocytes (Butt & Kalsi, 2006; Newman, 1986; Somjen, 1975; Wallraff et al., 2004), and are estimated to contact thousands of synapses (Bushong et al., 2002). These characteristics make them optimally suited for the uptake of K^+, allowing them to modulate neuronal excitability and avoid deleterious effects of locally prolonged increases in extracellular K^+ resulting from neuronal activity (for review see: Butt & Kalsi (2006)). Essential for the role of astrocytes in the clearance and redistribution of increased extracellular K^+ is

the inward rectifying K^+ channel Kir4.1. While its expression and function is normally tightly maintained, reactive astrocytes often show impaired Kir4.1 function leading to disturbed K^+ homeostasis and neuronal dysfunction under pathological conditions, as seen in epilepsy (Bedner & Steinhäuser, 2013; Dai et al., 2015; Ferraro et al., 2004) and Huntington's disease (Tong et al., 2014). Reduced Kir4.1 expression at the molecular level in reactive astrocytes further implicates an important role for K^+ buffering in AD progression (Wilcock et al., 2009). Moreover, since epilepsy and epileptiform activity (and thus neuronal hyper-excitability) are common phenomena in AD mouse models (Corbett et al., 2013; Del Vecchio et al., 2004; Gurevicius et al., 2013; Hazra et al., 2016; Minkeviciene et al., 2009; Palop et al., 2007) and have been reported in AD patients (Noebels, 2011; Rao et al., 2009; Vossel et al., 2013, 2016), understanding the contribution of astrocyte K^+ buffering in AD could help clarify potential underlying mechanisms contributing to network disturbances in this disease.

Previously published research showed a significant shift in gene expression of astrocytes, isolated from cortices of 15-month-old (15 M) to 18-month-old APP/PS1 mice, towards immune signaling and away from neuronal support functions (Orre, Kamphuis, Osborn, Melief, et al., 2014). Here we investigated whether this shift in molecular profile leads to changes in function and protein expression in astrocytes surrounding Aβ plaques. In particular, we aimed to determine if and how Kir4.1-mediated K^+ clearance is altered at the protein and physiological level. To answer this question, we chose 9-month-old (9 M) APP/PS1 mice where plaque distribution is prevalent enough in the dentate gyrus (DG) to allow systematic recording of plaque-associated astrocytes but also scarce enough to record from areas free of plaque deposition. The DG was picked so that we could evoke synaptic responses and measure subsequent K^+ currents in astrocytes. Using immunohistochemistry, we find that astrocytes in proximity of Aβ plaques in the middle molecular layer (MML) of the DG undergo distinct cytoskeletal changes and show localized increases in Kir4.1 protein expression. Additionally, we locally increased the extracellular K^+ concentration ($[K^+]_o$) to determine differences in Kir4.1 current density between plaque- and non-plaque-associated astrocytes in 9 M APP/PS1 mice. These experiments, combined with no apparent effect on astrocyte gap junction coupling efficiency, reveal that despite local increases in Kir4.1 protein expression, astrocyte K^+ buffering remains intact in early- to mid-stages of AD progression.

2 | MATERIALS AND METHODS

2.1 | Mice

Heterozygous double-transgenic APPswePS1dE9 mice (APP/PS1) (Jankowsky et al., 2004) and their wild type (WT) age-matched littermates of either sex were studied. Mice were originally received from Dr. Borchelt and backcrossed onto C57BL/6. APP/PS1 mice were maintained as hemizygotes by crossing with C57BL/6 mice (Harlan).

Genotype was determined by performing real-time polymerase chain reaction (PCR) with primers targeted to two transgenes expressed by the APP/PS1 mice -human/mouse chimeric APP with K595N/M596L Swedish mutation and human PS1 carrying the exon 9 deletion. For further details on this transgenic line, see also The Jackson Laboratory (strain B6.Cg-Tg(APPswe, PSEN1dE9)85Dbo/Mmjax; strain #034832-JAX; https://jaxmice.jax.org/). Animals were housed under standard conditions and were provided ad libitum food and water. All experiments were performed following protocols and guidelines approved by the Institutional Animal Care and Use Committee (UvA-DEC/IvD Utrecht) operating under standards set by EU Directive 2010/63/EU.

2.2 | Immunohistochemistry

To stain for astrocytes, oligodendrocytes, Aβ and Kir4.1, snap-frozen brain tissue from 3-month-old (3 M), 9 M, and 15 M APP/PS1 mice and WT littermates was used for immunohistochemistry. Coronal sections (12 μm) containing both hippocampus and cortex were thaw-mounted on Superfrost Plus slides (Thermo Scientific) and stored at −20°C until the day of staining. Sections were post-fixed in 4% paraformaldehyde (PFA) in phosphate-buffered saline (PBS; 13.7 mM NaCl, 0.27 mM KCl, 0.81 mM Na_2HPO_4, 0.15 mM KH_2PO_4, pH 7.4) at room temperature (RT), washed with PBS and then blocked for 1 h at RT with PBS supplemented with 10% normal donkey serum (NDS) and 0.4% Triton X-100. Sections were incubated overnight at 4°C with a combination of primary antibodies against GFAP (Sigma-Aldrich Cat# G3893, RRID: AB_477010, 1:4000), Olig2 (Millipore Cat# ab9610, RRID: AB_570666, 1:500), Kir4.1 (Alomone Labs Cat# APC-035, RRID: AB_2040120, 1:1800), and AB6E10 (Covance Cat# SIG-39300-500, RRID:AB_662807, 1:15000). Slices were subsequently incubated for 2 h with secondary Alexa488-, Alexa594- and Cy3-conjugated antibodies (1:1000) and imbedded in Vectashield Antifade Mounting Medium with DAPI (Vectorlabs, H-1200). Samples used to assess and quantify Kir4.1 expression were imaged with a Zeiss Axio-Scope A1 microscope at 20× magnification with a 1392 × 1040 pixel resolution. Additional images providing a detailed overview of Kir4.1 immunofluorescence, as depicted in Figure 4c and S2, were obtained using a confocal laser-scanning microscope (Zeiss, LSM880) at 63× magnification, with a 1024 × 1024 pixel resolution and 1 AU pinhole diameter using a 1-μm step size.

To stain biocytin-filled astrocytes, slices used for patching were washed in PBS and subsequently blocked using the same method as described above. Slices were then incubated overnight with a primary antibody against GFAP (Agilent Cat# Z0334, RRID:AB_10013382, 1:1500) and a streptavidin-Alexa594-conjugated secondary antibody (Invitrogen, Cat# S11227, 1:1000). The next day, slices were incubated for 2 h with a secondary Alexa488-conjugated antibody (1:1000) against GFAP, subsequently stained with Hoechst nuclear staining (Thermo Fisher Scientific Cat# H3569, RRID:AB_2651133, 1:200) and finally mounted on microscopy glasses using FluorSave

Reagent (Merck Millipore, 345789). A confocal laser-scanning microscope (Zeiss, LSM880) was used for imaging slices to determine astrocyte reactivity and gap junction coupling efficiency. Images were obtained at 20× magnification, with a 1024 × 1024 pixel resolution and 1 AU pinhole diameter. To assess astrocyte tracer coupling, z-stacks were taken at 2-μm step size. Cells were counted using the ImageJ cell counter plugin (Schindelin et al., 2012). To ascertain quantification of biocytin-filled astrocytes, cells were only included in analysis when positive for both biocytin and GFAP. Images of biocytin$^+$/GFAP$^+$ cells were recounted by another observer blinded to the experimental conditions and cell counts were subsequently averaged across both observers before statistical data analysis.

2.3 | Quantitative polymerase chain reaction

GFAP expression levels were quantified with PCR on RNA isolated from hippocampal homogenates of APP/PS1 mice and WT littermates. In brief, total isolated RNA was first treated with DNase I and then used to generate complementary DNA (cDNA) (Quantitect-Qiagen) using Oligo(dT) and random hexamer primers. cDNA was further diluted 1:20 and used as a template for quantitative PCR (SYBR Green PCR Master Mix; Applied Biosystems). The differential expression of GFAP was probed using a forward (5′-GGAGATGCGGGATGGTGAG-3′) and a reverse primer (5′-ACCACGTCCTTGTGCTCCTG-3′). Transcript expression was normalized to the geometrical mean of three reference genes (Gapdh, Actb, Hprt) from the same cDNA pool, as described before (Kamphuis et al., 2012).

2.4 | Magnetic-activated cell sorting and RNA sequencing

To assess Kir4.1 mRNA expression in the hippocampus and cortex of APP/PS1 and WT littermates, mice were anesthetized with 0.1 ml Euthanimal 20% (Alfasan 10020 UDD) and transcardially perfused with 1× PBS. Brains were dissected and the hippocampus and cortex were collected. Six hippocampi or six cortices obtained from three animals were then pooled as a single sample for further processing. Tissue was dissociated both mechanically and by using enzymatic digestion with Papain (Interchema C.V.-Antonides, LS003126) and DNAse (Sigma-Aldrich, 0104159001). MS columns (Miltenyi biotec, 130-042-201) were used for magnetic-activated cell sorting (MACS). Cells were first incubated with CD11b Microbeads (Miltenyi biotec, 130-049-601) to capture microglia, and next incubated first with FcR blocking reagent and then Asca-1 Microbeads (Miltenyi biotec, 130-097-678) to sort astrocytes. Sorted astrocytes were stored in Trizol (Qiagen, 79306) at −80°C until further use. RNA was isolated by using Chloroform and isoporopanol, and then further purified and concentrated with magnetic beads (Deckman Coulter, AM PureXP A63881). The RNA integrity number (RIN) and concentration were determined with Pico chip analysis (Agilent RNA 6000 Pico Kit,

5067-1513). RNA was reversed transcribed to DNA with a reverse transcription kit (Qiagen, 205311). DNA was then sent to Single Cell Discoveries (B.V. in Utrecht, https://www.scdiscoveries.com/) for bulk RNA sequencing. Sequencing data was analyzed with the DESeqDataSetFromMatrix R script.

2.5 | Slice preparation and electrophysiology

Acute horizontal slices (290 μm) of the ventral hippocampus were obtained from 270–290 days old APP/PS1 mice and WT littermates. Mice were decapitated and the brain was rapidly removed into ice-cold oxygenated (95% O_2–5% CO_2) slicing artificial cerebrospinal fluid (aCSF; 87 mM NaCl, 60 mM sucrose, 2.5 mM KCl, 1.25 mM NaH_2PO_4, 7 mM $MgCl_2$, 0.5 mM $CaCl_2$, 10 mM D-glucose, 25 mM $NaHCO_3$, pH 7.4). Slices were cut with a vibratome (VT1000S) and transferred to slicing aCSF of 35°C for 20 min. Sulforhodamine 101 (SR101; 1 μM, S7635, Sigma) was added and the slices were incubated for 20 min at 35°C to selectively stain astrocytes (Schnell et al., 2015). Next, slices were transferred to aCSF (126 mM NaCl, 3 mM KCl, 2 mM $CaCl_2$, 2 mM $MgSO_4$, 1.25 mM NaH_2PO_4, 26 mM $NaHCO_3$, 10 mM D-glucose, pH 7.4) and continuously oxygenated with 95% O_2–5% CO_2. Additionally, before performing Kir4.1 current recordings, slices were placed for 12 min in aCSF that also contained Methoxy-X04 (10 μM in 0.01% DMSO, cat. #4920, Tocris) to visualize Aβ-plaque deposits (Klunk et al., 2002). Miniature excitatory postsynaptic currents (mEPSCs) were recorded in the presence of 1 μM tetrodotoxin (TTX). The recording chamber was continuously perfused with aCSF (2.5 ml/min) and kept at 28°C.

Whole-cell voltage and current-clamp recordings were obtained from astrocytes in the MML and neurons in the granule cell layer (GCL) of the DG with an Axopatch 200B (Axon Instruments). Neurons and astrocytes were voltage-clamped at −70 mV and −80 mV, respectively. Directly after break-in, cells were allowed to rest for 5 min for the recording to stabilize. Recording pipettes were pulled from borosilicate glass (Science Products) and had resistances of 3–5 MΩ. For Kir4.1 current density, pipette solution contained 136 mM K⁺ D-gluconate, 10 mM NaCl, 10 mM 2-[4-(2-hydroxyethyl)piperazin-1-yl]ethanesulfonic acid (HEPES), 0.5 mM ethylene glycol-bis(2-aminoethylether)-N,N,N′,N′-tetraacetic acid (EGTA), 5 mM Mg-ATP, 0.5 mM Na_2-GTP, pH adjusted to 7.3. For mEPSC recordings, pipette solution contained 139 mM CsMSF, 5 mM CsCl, 2 mM $MgCl_2$, 0.2 mM EGTA, 10 mM HEPES, 10 mM creatine phosphate, 4 mM Na_2-ATP, 0.3 mM Na_3-GTP, pH adjusted to 7.3. mEPSC recordings from GCL neurons were obtained over a 7-min period. The frequency was calculated over a 2-min period. In astrocytes, the response to 10 mV voltage steps in uncompensated voltage-clamp configuration was used to determine membrane resistance, cell capacitance, series resistance and resting membrane potential according to the method described by (Akopian et al., 1997). This allowed for offline correction of voltage error and was used in subsequent figures to report voltage values. The Kir component of the K⁺ current was isolated by washing in 100 μM $BaCl_2$ (Coetzee et al., 1999). Whole-cell and Kir4.1 chord conductance (G_m) were calculated at resting membrane potential (∼−80 mV) according to:

$$G(V_m) = \frac{I(V_m)}{V_m - E_{rev}},$$

with V_m being the membrane potential and E_{rev} the reversal potential of K⁺, in our case 101.9 mV. To evoke synaptic responses, a 0.2 ms bi-phasic current pulse (Digitimer) was given by locating a bipolar tungsten electrode (WPI) to the perforant path (PP) at a distance of up to 300 μm from the recorded cell. Evoked astrocyte responses were recorded after either a single current pulse or a tetanic stimulus of 1 s at 100 Hz at half-maximal response intensity, repeated three times at 4-s intervals. K⁺ puffs were generated by replacing 7 mM NaCl with 7 mM KCl in aCSF and subsequently administered through a micropipette by a brief (50 ms) pressure pulse (10 psi) applied from a Picospritzer (General Valve). Control recordings were performed to exclude an effect of mechanical stimulation.

To assess astrocyte gap junction coupling efficiency, 0.5% biocytin (Sigma-Aldrich, B4261) was added to a K⁺-gluconate-based pipette solution (130 mM K⁺ D-gluconate, 1 mM $MgCl_2 \times 6H_2O$, 20 mM HEPES, 10 mM EGTA, 3 mM Na_2-ATP, pH adjusted to 7.2). A single astrocyte per brain slice was patched for 20 min to allow for passive diffusion of biocytin through the astrocyte syncytium. After 20 min, slices were fixed overnight in 4% PFA in PBS and subsequently stored in PBS until further processing.

In all experiments, cells were visualized with an upright microscope (SliceScope Pro 6000, Scientifica) equipped with oblique illumination and a 40× water immersion objective. Astrocytes were visually identified by their small soma size and irregular shape and were checked for SR101 positivity using a 585 nm LED (pE-100, CoolLED) and mCherry-Texas Red filter cube (Chroma). Data acquisition and analysis were performed with either in-house software running in Matlab (MathWorks) (Kir4.1 current density exp.) or Axon pCLAMP10 (Molecular Devices) (astrocyte gap junction coupling efficiency exp.). Signals were filtered at 2 kHz and sampled at 20 kHz using an NI USB-6259 digitizer (National Instruments). Liquid junction potential (−14 mV) was corrected online. Series resistance and cell capacitance were monitored during recording and cells were excluded from analyses when values fluctuated >10%.

2.6 | Statistics

Reported numerical values are given as mean and standard error of the mean (±SEM), unless mentioned otherwise. Statistical analyses were performed using GraphPad Prism Version 6. Prior to group comparison, outliers were identified using the build-in GraphPad Prism outlier identifier (ROUT, $Q = 1\%$). Comparisons between two groups were made using a two-tailed unpaired Student's t-test. Comparisons of more than two groups were performed with a one-way or two-way analysis of variance (ANOVA). Normality of data was tested with the D'Agostino-Pearson test. When data were not normally distributed or

when an *F*-test or Bartlett's test for homogeneity of variances indicated unequal variances between groups, non-parametric equivalents were used. The statistical test used for each comparison is indicated in the Results section. Post hoc multiple comparison tests to determine group differences were used where appropriate and are indicated when relevant. For all statistical evaluations, we assumed that $p < 0.05$ indicates rejection of the null hypothesis. The number of cells and mice used for analyses are indicated at the relevant comparison by '*n*' and '*N*', respectively.

3 | RESULTS

3.1 | Astrocytes undergo cytoskeletal changes and surround Aβ plaques in the MML of the DG

AD is characterized by astrocytes becoming increasingly reactive throughout disease progression affecting both their appearance and function. Alterations in astrocyte morphology and the increased expression of GFAP are commonly used to differentiate reactive astrocytes from their healthy counterparts (Hol & Pekny, 2015). To confirm the presence of astrocyte reactivity in the DG MML of 9 M APP/PS1 mice, as well as to determine their primary location, we performed immunohistochemistry on coronal brain slices targeting both GFAP and Aβ plaques. Results indicate that astrocytes undergo clear cytoskeletal changes when exposed to Aβ plaque pathology (Figure 1a). Whereas in some brain regions astrocyte reactivity appears to be homogeneously distributed, our results suggest that cytoskeletal changes in astrocytes are especially prevalent in close proximity to Aβ plaques, as demonstrated by the astrocytes encapsulating the Aβ plaque and their distinct interaction with the plaque core. These findings suggest a reactive state in astrocytes that reside near Aβ plaques in the DG MML in 9 M APP/PS1 mice.

While the presence of astrocyte reactivity in AD has widely been indicated throughout the literature, its consequences for astrocyte function and protein expression remain relatively unclear. Particularly important for the regulation of ion homeostasis by astrocytes is the inward rectifying K$^+$ channel Kir4.1. Given that Kir4.1 is crucial for the normal K$^+$ buffering capacity of astrocytes, in combination with various studies (Bedner & Steinhäuser, 2013; Dai et al., 2015; Ferraro et al., 2004) indicating that astrocytes often show disturbances in K$^+$ homeostasis due to impaired Kir4.1 function under pathological conditions, the main question we asked here was whether also in AD, astrocyte reactivity is associated with changes in Kir4.1 expression and function.

3.2 | Kir4.1 protein expression is locally increased in APP/PS1 astrocytes in cortex and hippocampus

To assess the expression pattern of Kir4.1 protein we used immunohistochemistry. Although primarily interested in the hippocampus and cortex of 9 M mice, we also included the hippocampus and cortex of 3 M and 15 M APP/PS1 mice in our analysis to assess brain region differences in Kir4.1 expression patterns during AD pathogenesis. Overall, staining for Kir4.1 was diffuse and densely distributed throughout the WT cortex and hippocampus, often showing increased expression surrounding blood vessels (Figure 2a,b; 3a,b, white asterisks, top plates). In 3 M old APP/PS1 mice, the Kir4.1 protein expression pattern strongly resembled the expression pattern seen in WT littermates, suggesting that pre-pathology astrocytes resemble the non-pathological state when it comes to Kir4.1 protein expression in both the cortex and hippocampus (Figure 2a,b; 3a,b; left plates). This expression pattern changed with the appearance of age-related Aβ plaque pathology. The distribution of Kir4.1 staining was patchier and concentrated near Aβ plaques and vasculature in the cortex and hippocampus of 9 M and 15 M APP/PS1 mice (Figure 2b; 3b, middle and right panels). Layers of the somatosensory cortex and the location of Aβ plaques were visible in the DAPI channel. Kir4.1 protein was upregulated surrounding Aβ plaque pathology, both in the cortex (Figure 2b, white arrows middle and right panels) and particularly in hippocampal tissue sections (Figure 3b, white arrows middle and right panels) of the 9 M and 15 M age groups. This increase in Kir4.1 staining correlated with plaque pathology and the presence of GFAP$^+$ astrocytes in all age groups we studied. Furthermore, astrocytes characterized by high levels of GFAP expression were present in cortical and hippocampal APP/PS1 tissue and increased from 9 M to 15 M (Figure 2b, middle and right panels, green). This was particularly noticeable in cortical tissue as the expression of GFAP in cortical astrocytes under non-pathological conditions is low. Additional quantitative PCR data demonstrating increased GFAP expression levels in the hippocampus is provided in the supplementary figures (Figure S1).

To verify that Kir4.1 is locally upregulated surrounding Aβ plaques, we quantified Kir4.1 staining by determining average gray values in the Kir4.1 channel in 5–10 μm concentric shells surrounding Aβ plaques up to 100 μm distance. Kir4.1 immunofluorescence showed significantly enhanced mean fluorescence within 40 and 30 μm of the center of an Aβ plaque in the cortex (Figure 4a, two-way ANOVA, group: $p < 0.0001$, distance: $p < 0.0001$, interaction: $p = 0.0004$; Bonferroni's: 9 M ($n = 27$, $N = 5$); 0–5, $p = 0.1038$; 5–10, $p = 0.0016$; 10–15, $p = 0.0206$. 15 M ($n = 32$, $N = 6$); 0–5, $p < 0.0001$; 5–10, $p < 0.0001$; 10–15, $p < 0.0001$; 15–20, $p < 0.0001$; 20–30, $p < 0.0001$; 30–40, $p = 0.0284$) and DG (Figure 4b, two-way ANOVA, group: $p = 0.1884$, distance: $p < 0.0001$, interaction: $p = 0.8915$; Bonferroni's: 9 M ($n = 17$, $N = 5$); 0–5, $p = 0.0001$; 5–10, $p < 0.0001$; 10–15, $p < 0.0001$; 15–20, $p < 0.0001$; 20–30, $p = 0.0054$. 15 M ($n = 16$, $N = 6$); 0–5, $p = 0.0819$; 5–10, $p < 0.0001$; 10–15, $p < 0.0001$; 15–20, $p = 0.0035$), respectively. Beyond these regions, intensity tapered off to background immunofluorescence, as defined at 80–100 μm from the center of the plaque. The same analysis showed increased Kir4.1 fluorescence in the proximity of Aβ plaques in the cortex but not in the DG of 15 M mice compared to 9 M mice (Figure 4a,b). To average over multiple preparations, all values within a single image were normalized to the mean value of a concentric shell at 80–100 μm from the plaque center, which was considered to resemble 'background'
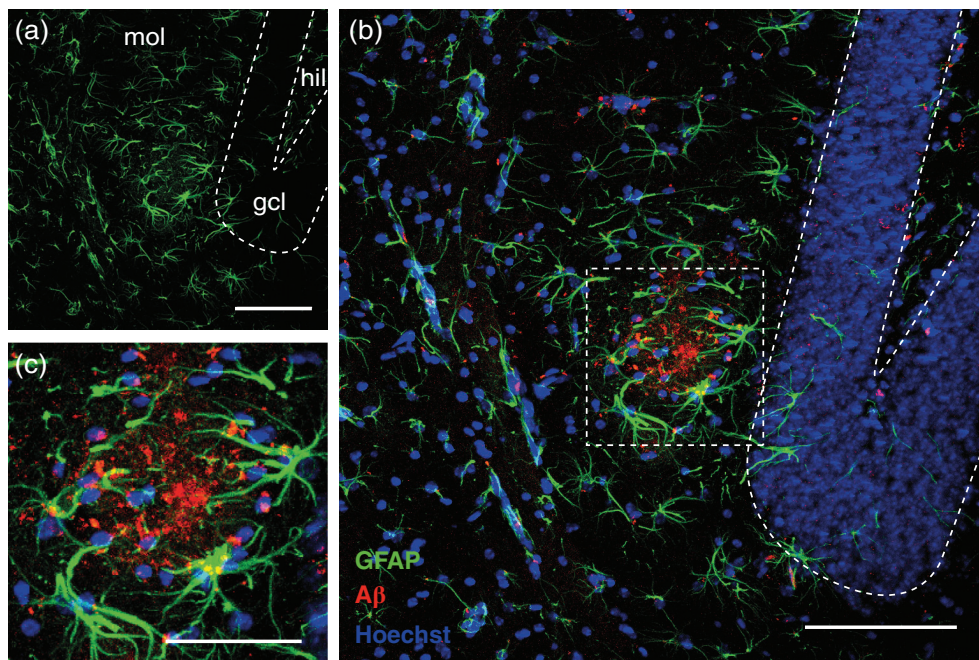
FIGURE 1   Astrocytes surrounding Aβ plaques in the DG MML of 9 M APP/PS1 mice show clear cytoskeletal alterations. (a) GFAP staining showing astrocytes in the DG MML of 9 M APP/PS1 mice. Astrocytes alone reveal the location of the Aβ plaque. Scale bar: 100 μm. (b) Merged image showing astrocytes in green (GFAP), the Aβ plaque in red (6E10) and nuclei in blue (Hoechst). Astrocytes display alterations in their GFAP cytoskeleton and enclose the Aβ plaque deposit. The dashed square depicts the zoomed-in area shown in c. scale bar: 100 μm. (c) Enlargement of the astrocytes enclosing the Aβ plaque. Scale bar: 50 μm. Dashed lines indicate brain regions; gcl, granule cell layer; hil, hillus; mol, molecular layer

immunofluorescence. Subsequent confocal image analysis revealed that Kir4.1 expression proximal to Aβ plaques largely localizes to GFAP$^+$ astrocytes (Figure 4c), and only rarely to other Kir4.1-expressing cells, such as oligodendrocytes (Figure S2). The spongiform morphology of an astrocyte positive for GFAP was clearly visible adjacent to a deposition of Aβ (Figure 4c, white asterisks). Z-stacks of a 12-μm cryo-section obtained from a 9 M APP/PS1 mouse revealed co-localization of the signals for GFAP and Kir4.1 in two different astrocytes proximal to two separate plaques in the DG (Figure 4c, coordinates x1, y1 and x2, y2). This confocal image further highlights the heterogeneity of Kir4.1 expression in the DG, as can be observed by the variation in Kir4.1 expression pattern surrounding the two Aβ plaques. Additional analysis revealed no significant difference between Kir4.1 mRNA expression in MAC-sorted hippocampal and cortical astrocytes of 9 M APP/PS1 mice and WT littermates (Figure S3).

Together, these results show that exposure of astrocytes to Aβ plaques in AD coincides with the local upregulation of specifically Kir4.1 protein expression, possibly compensating for an alteration in K$^+$ ion buffering towards areas with higher plaque burden.

3.3 | Kir conductance in hippocampal astrocytes surrounding Aβ plaques is unaltered

To investigate whether a local upregulation of Kir4.1 protein expression in plaque-enriched areas also has functional consequences,

electrophysiological properties of astrocytes of 9 M APP/PS1 mice and their WT littermates were studied. At this age, there are numerous plaques present in the DG as well as considerable plaque-free areas, enabling recordings from astrocytes close to as well as further away from plaques. Astrocytes of the DG MML positive for SR101 were recorded in whole-cell configuration (Figure 5a). The basal membrane characteristics of 9 M astrocytes matched characteristics described in the literature including low membrane resistance, resting membrane potential close to the K$^+$ equilibrium potential, and a linear current–voltage (IV) relationship around resting potential (Table 1, Figure 5b).

The average resting membrane potential did not differ between cells recorded in WT and APP/PS1 mice (Table 1). Kir4.1 chord conductance of WT and APP/PS1 astrocytes was then determined for each individual IV-relationship around resting membrane potential (Table 1). None of these electrophysiological properties showed a significant difference between astrocytes in APP/PS1 and WT mice.

APP/PS1 astrocytes were then split into two groups based on their proximity to visible Aβ plaques, identified by positive staining for methoxy-X04 (Figure 5c, blue) and/or their characteristic appearance under bright-field illumination. Astrocytes up to 80 μm away from an Aβ plaque undergo distinct phenotypic and morphological changes (Bouvier et al., 2016; Galea et al., 2015; Serrano-Pozo et al., 2013). Therefore, proximal astrocytes were defined as <80 μm of a plaque, while distal astrocytes were located at a distance of >100 μm to a visible plaque. Although brain slices were 290 μm thick, we cannot exclude that superficial astrocytes and nearby plaques were separated
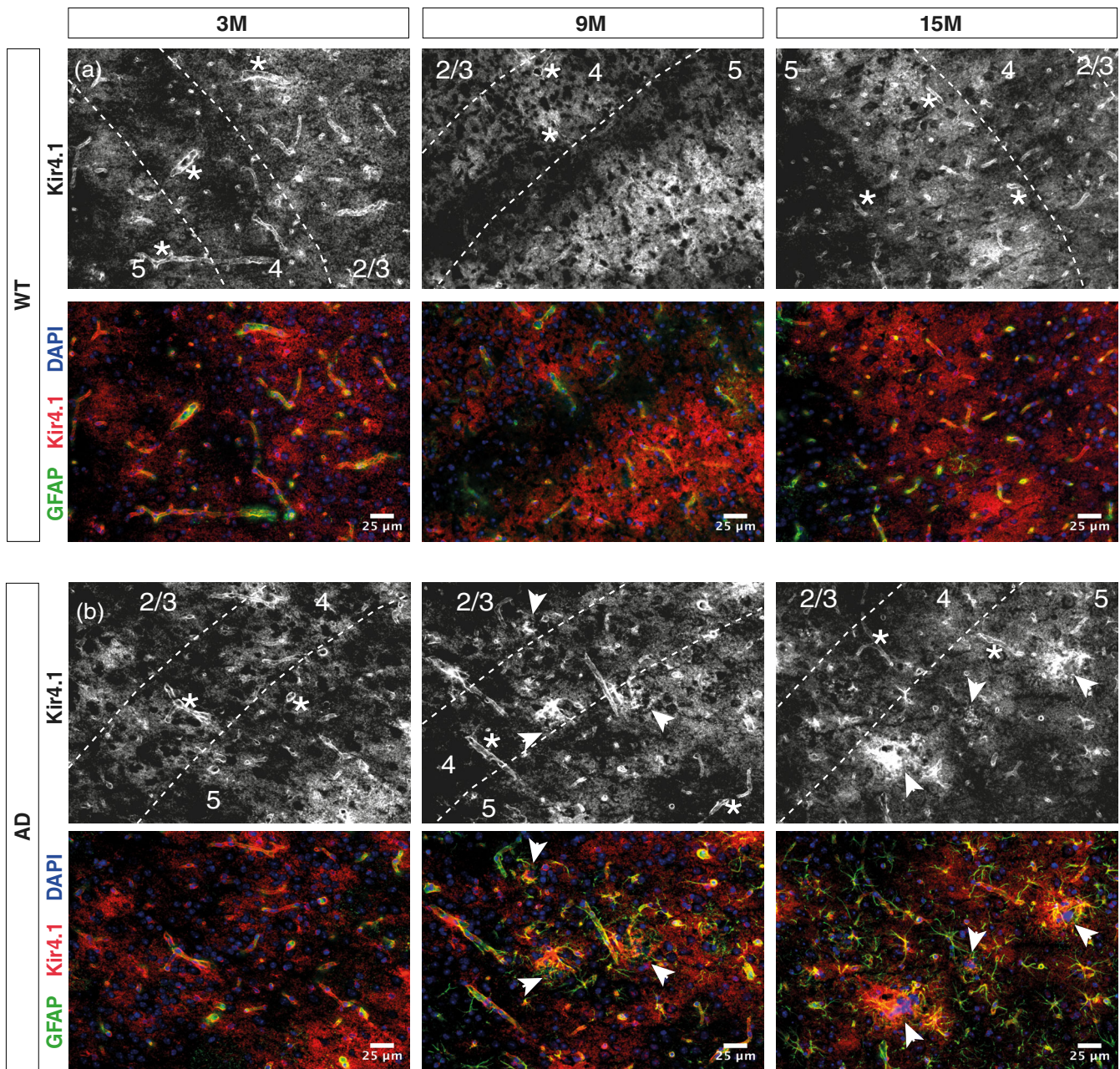
FIGURE 2 Neocortical expression of Kir4.1 is locally increased surrounding Aβ plaques. (a) In the somatosensory cortex of WT mice Kir4.1 expression (represented as intensity in the b/w plates and in red in the colored plates) was relatively consistent across 3 M, 9 M, and 15 M cortices. Expression of Kir4.1 appeared to be somewhat stratified with lower expression at the border of layer 4 and 5 and a distinct band of expression within layer 5; this was more obvious in 9 M and 15 M mice (cortical layers delineated by white lines and layer numbers). GFAP expression (green) was largely undetectable in 3 M mice and is more prevalent, though sparse, in 9 M and 15 M mice. Kir4.1 staining is increased surrounding blood vessels (white asterisks). (b) In the somatosensory cortex of APP/PS1 mice Kir4.1 expression (represented as intensity in the b/w plates and in red in the colored plates) showed a similar distribution pattern in 3 M pre-pathology APP/PS1 animals when compared to controls. Kir4.1 expression was locally increased surrounding plaques. The location of plaques was determined in the DAPI channel (blue), and are represented by white arrows in the middle and right plates; plaques were absent in WT littermates and 3 M APP/PS1 mice. Kir4.1 was still visible surrounding blood vessels (white asterisks). GFAP expression was also characteristically increased surrounding Aβ plaque pathology and is virtually absent in the cortex of pre-pathological APP/PS1 mice. Scale bar: 25 μm

by slicing. Distinguishing between proximal and distal APP/PS1 astrocytes revealed no significant differences in passive membrane properties related to location in respect to plaques (Table 1, Figure 5d).

Series resistance (R_s), membrane capacitance (C_m), resting membrane potential (V_m) and membrane chord conductance (G_m) were all similar between proximal and distal astrocytes (Table 1).
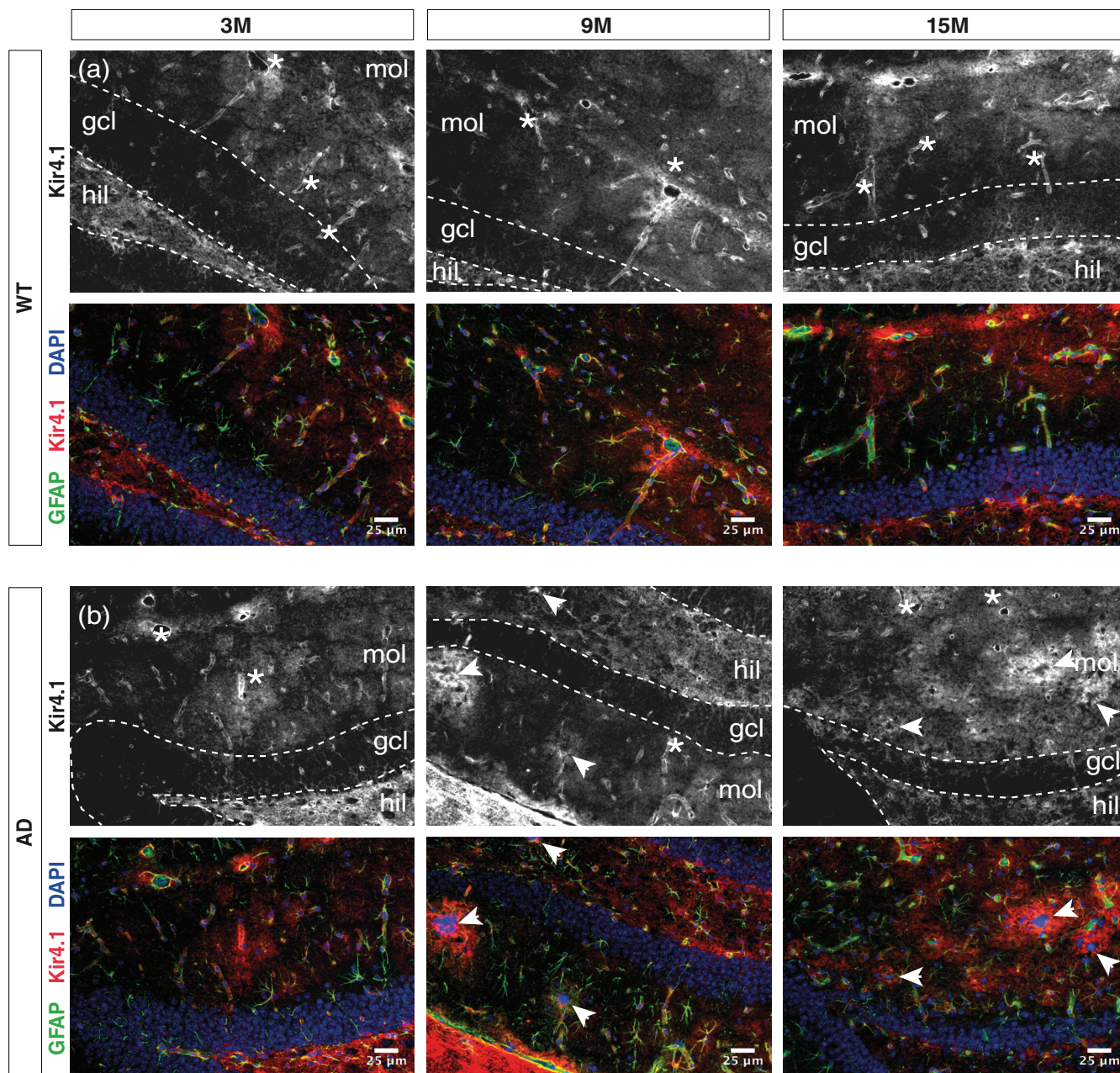
FIGURE 3 Hippocampal expression of Kir4.1 is locally increased surrounding Aβ plaques. (a) In the DG of WT mice, Kir4.1 expression (represented as intensity in the b/w plates and in red in the colored plates) was relatively consistent across 3 M, 9 M, and 15 M mice. Expression of Kir4.1 appeared increased surrounding blood vessels (white asterisks). GFAP expression (green) was visible in 3 M, 9 M, and 15 M WT mice. (b) In the DG of APP/PS1 mice, Kir4.1 expression (represented as intensity in the b/w plates and in red in the colored plates) showed a similar distribution pattern in 3 M pre-plaque pathology APP/PS1 mice when compared to controls with increased expression in surrounding blood vessels (white asterisks). The location of plaques was determined in the DAPI channel (blue), and are represented by white arrows in the middle and right plates; plaques were absent in WT littermates and 3 M APP/PS1 mice. Kir4.1 expression was locally increased surrounding plaques of 9 M (middle plates) and 15 M (right plates) APP/PS1 mice. GFAP expression was also characteristically increased surrounding plaque pathology, though expression in the hippocampus was apparent in both APP/PS1 mice and WT littermates of all age groups. Scale bar: 25 μm

3.4 | No difference in Ba^{2+}-sensitive currents in 9 M APP/PS1 compared to WT astrocytes

To determine whether a shift in Kir4.1 protein expression pattern was associated with disturbed Kir4.1 functionality, Ba^{2+}-sensitive currents were isolated in APP/PS1 and WT astrocytes. Low concentration (100 μM) of Ba^{2+} was washed in after initial whole-cell patch-clamp recordings were established. The difference in IV-relationships before and during wash-in revealed the Ba^{2+}-sensitive current (Figure 6a–c), which was quantified by the chord conductance around resting
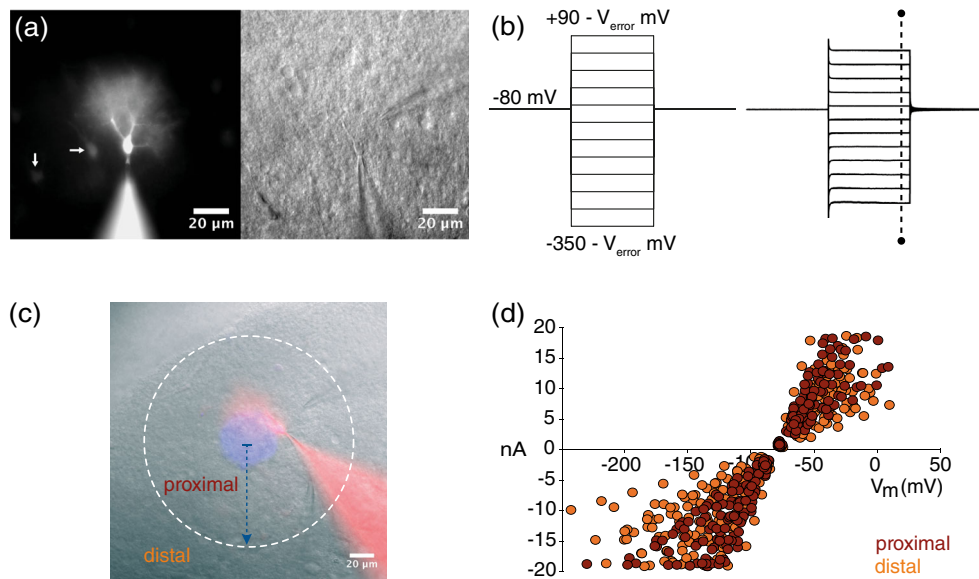
FIGURE 4 Legend on next page.

FIGURE 5 Electrophysiological characterization of whole-cell patch-clamped astrocytes in the MML of the DG. (a) Patched SR101$^+$ astrocyte filled with Alexa 568 (40 μM) showed spongiform morphology of the fine processes with larger processes extending from the soma. Additionally, some SR101$^+$ astrocytes can be seen surrounding the filled astrocyte (out of focal plane). The bright-field image shows the K$^+$ puff pipette to the upper right of the patch electrode. (b) Patched astrocytes were voltage-clamped at −80 mV holding potential and stepped to varying potentials between −350 and 90 mV for 50 ms before correcting for series resistance offline and the resulting current response was determined at 45 ms after the voltage-step, example trace shown. (c) Astrocytes were classified by their proximity to the nearest visible Aβ plaque labeled with methoxy-X04 (blue) or visible in bright-field illumination, <80 μm for proximal and >100 μm for distal astrocytes. (d) The chord conductance did not significantly differ between groups. Proximal astrocytes had a chord conductance of 0.121 ± 0.009 μS and distal astrocytes of 0.112 ± 0.005 μS

TABLE 1 Membrane properties of patch-clamped astrocytes from 9 M APP/PS1 mice and WT littermates. APP/PS1 astrocytes in the DG MML generally show membrane characteristics similar to WT astrocytes. APP/PS1 astrocytes are further split into two subpopulations depending on their distance to the nearest visible plaque, proximal: within 80 μm or distal: further than 100 μm away

	C_m (pF)	V_r (mV)	R_m (MΩ)	R_s (MΩ)	G_m (μS)	G_m/C_m (nS/pF)	Ba^{2+} blocked (%), Figure 6
WT ($n = 33$, $N = 17$)	33.6 ± 1.8	−77.9 ± 0.4	4.3 ± 0.3	9.1 ± 0.4	0.115 ± 0.005	3.6 ± 0.2	29.7 ± 2.8 ($n = 15$, $N = 8$)
APP/PS1 ($n = 49$, N = 20)	34.5 ± 2.5	−77.3 ± 0.3	4.6 ± 0.4	9.3 ± 0.4	0.116 ± 0.005	4.1 ± 0.3	–
Proximal ($n = 22$, $N = 18$)	39.2 ± 4.0	−77.4 ± 0.4	4.2 ± 0.6	9.1 ± 0.5	0.121 ± 0.009	3.6 ± 0.4	25.6 ± 4.9 ($n = 11$, $N = 9$)
Distal ($n = 27$, $N = 15$)	30.6 ± 3.0	−77.3 ± 0.4	4.9 ± 0.4	9.4 ± 0.5	0.112 ± 0.005	4.4 ± 0.4	23.4 ± 4.1 ($n = 10$, $N = 6$)

Notes: Capacitance (C_m), resting membrane potential (V_r), membrane resistance (R_m), series resistance (R_s), chord conductance at V_r (G_m), normalized chord conductance (G_m/C_m) and fraction of current blocked by Ba^{2+} (Ba^{2+} blocked); this group is a subset of the total population, number of astrocytes in brackets. None of the differences were statistically significant ($p > 0.05$ for all comparisons).

membrane potential (Figure 6d). Chord conductance of the Ba^{2+}-sensitive current was similar in APP/PS1 and WT astrocytes (0.038 ± 0.005 μS) in both proximal (0.031 ± 0.007 μS) and distal (0.027 ± 0.005 μS) conditions (one-way ANOVA, Bonferroni's: WT ($n = 15$, $N = 8$) versus proximal ($n = 11$, $N = 9$), $p > 0.9999$; WT versus distal

($n = 10$, $N = 6$), $p = 0.5157$; proximal versus distal ($p > 0.9999$), also when normalized for cell capacitance (Figure 6e,f, one-way ANOVA, Bonferroni's: WT ($n = 15$, $N = 8$) versus proximal ($n = 11$, $N = 9$), $p > 0.9999$; WT versus distal ($n = 10$, $N = 6$), $p > 0.9999$; proximal versus distal ($p > 0.9999$). The fraction of conductance blocked by

FIGURE 4 Quantification of Kir4.1 staining and confocal image analysis shows increased Kir4.1 expression surrounding Aβ plaques. (a) In the cortex, both 9 M and 15 M mice showed increased Kir4.1 staining up to 40 μm from the plaque center. Additionally, Kir4.1 staining was significantly increased in 15 M compared to 9 M APP/PS1 mice. (b) In the DG, both 9 M and 15 M mice showed increased Kir4.1 staining up to 30 μm from the plaque center. Dashed line indicates baseline fluorescence at 80–100 μm from plaque center. Bright-colored data points are significantly different from dashed line. (c) Z-stacks show Kir4.1 staining (green) co-localizing with and surrounding GFAP filament staining (red). The image shows one section from a confocal z-stack with x1 and y1 corresponding to all z-stacks along the yellow grid lines and x2 and y2 corresponding to all z-stacks along the white grid lines. The grid lines are centered over individual GFAP$^+$, astrocyte filament bundles proximal to Aβ-plaques (DAPI, white asterisk) to reveal colocalization of the red GFAP signal with the green Kir4.1 signal. GFAP filament staining only partially represented the full volume of an astrocyte and is not present in the fine filopodia of these cells where Kir4.1 protein was located. Statistical differences between groups are indicates with asterisks; **: $p < 0.01$, ***: $p < 0.001$
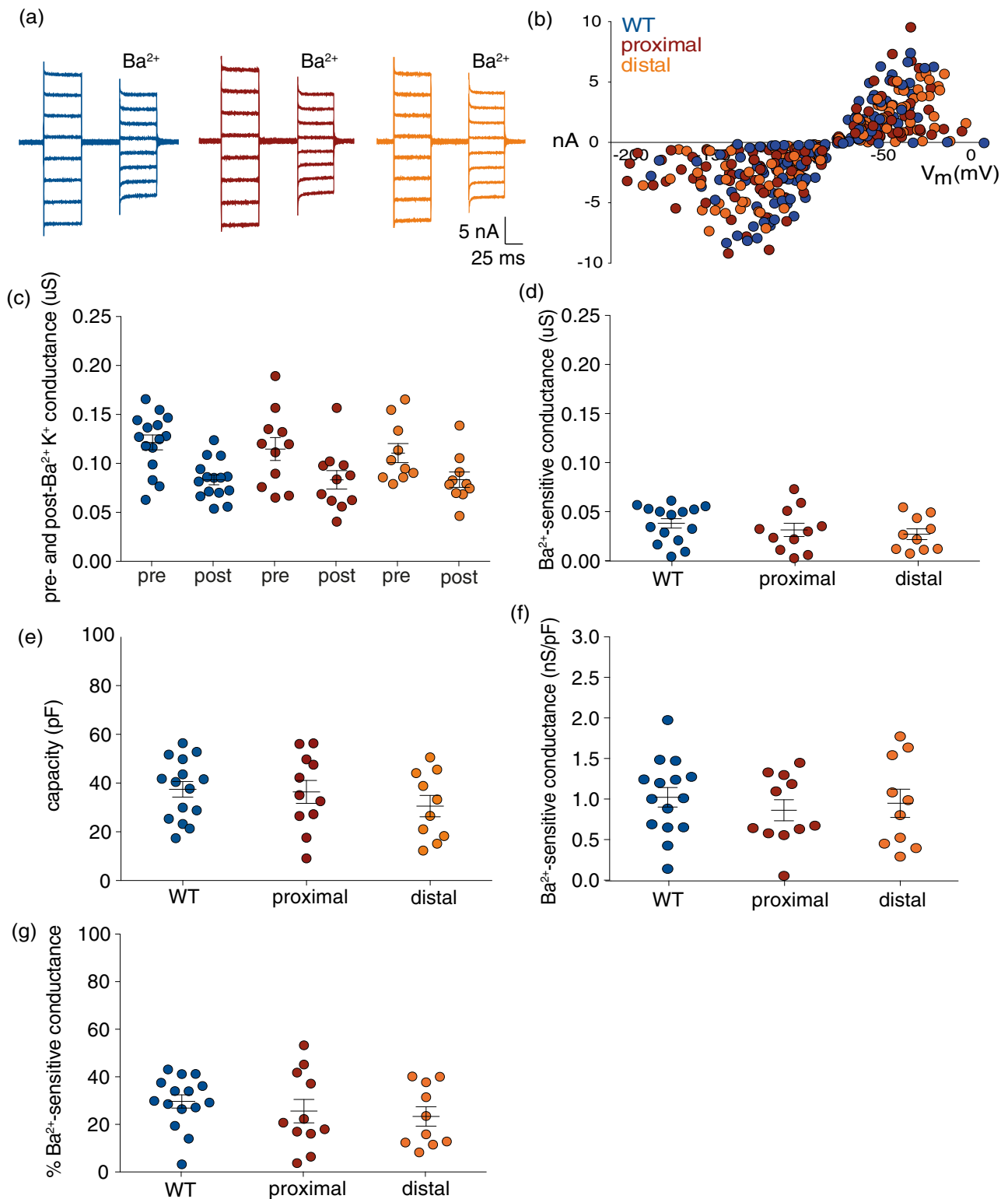
FIGURE 6 Isolated inward rectifier current in APP/PS1 and WT astrocytes after wash-in of Ba^{2+}. (a) K^+ currents in APP/PS1 and WT astrocytes were recorded before and during wash-in of 100 μM Ba^{2+}, revealing the Kir current component. Left and right IV traces indicate K^+ currents pre and post Ba^{2+} wash-in, respectively. IV traces from WT, proximal, and distal astrocytes are depicted in blue, red, and orange, respectively. (b) IV relationship of the isolated Kir currents. (c) K^+ chord conductance pre and post Ba^{2+} wash-in around resting membrane potential (−90 to −70 mV). (d) Ba^{2+}-sensitive chord conductance around resting membrane potential (−90 to −70 mV) was calculated from the data in (b). None of the differences between groups reached significance. (e) Cell capacitance was determined from the uncompensated voltage step responses (see Section 2) and was similar between all groups (WT, 37.5 ± 3.2 pF; proximal, 36.4 ± 4.7 pF; distal, 30.6 ± 4.4 pF). (f) Ba^{2+}-sensitive chord conductance normalized to cell capacitance was also similar between groups. (g) The percentage of Ba^{2+}-sensitive conductance indicates the fraction of total K^+ conductance attributable to Kir and was not significantly different between groups
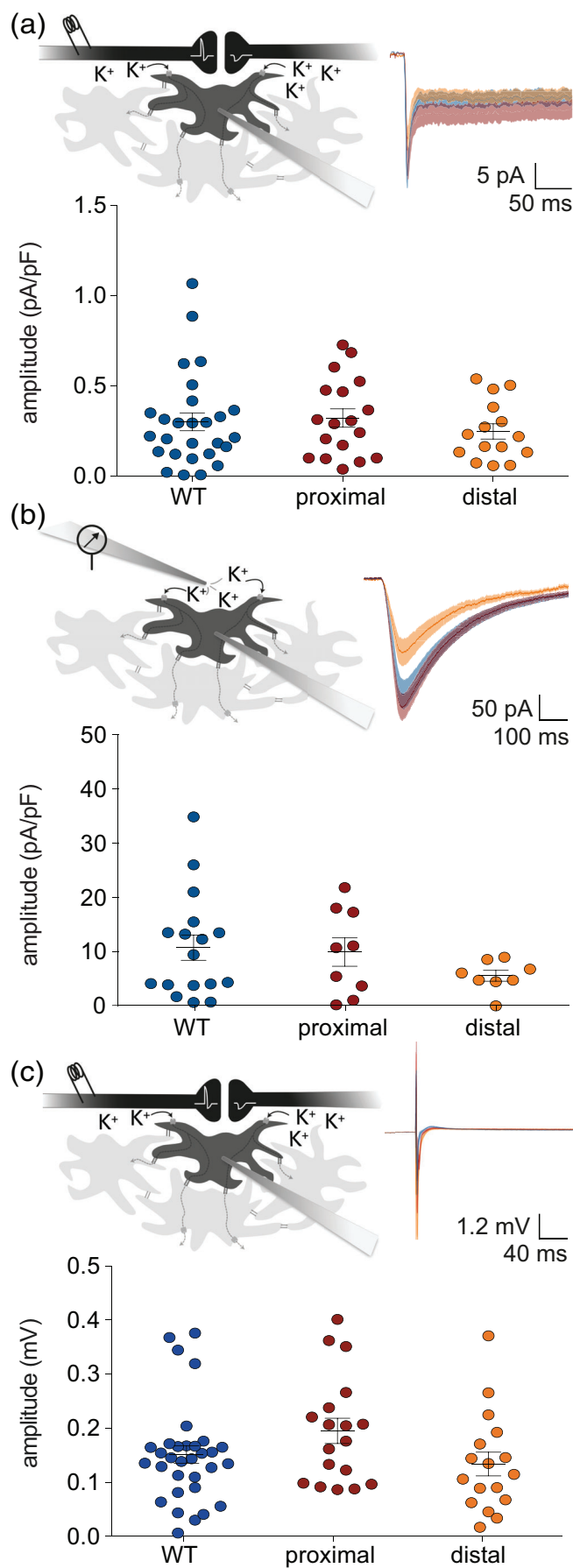
Ba^{2+} amounted to around 26% of the total conductance in all groups (Figure 6g, Table 1). Although astrocytes showed a considerable variation in Kir current amplitudes, we did not observe any difference between WT and APP/PS1 astrocytes or proximal and distal astrocytes.

3.5 | Evoked inward current in astrocytes reveals local differences in response to PP stimulation and high K$^+$ application

Next, we studied whether astrocytes exposed to Aβ plaques displayed differences in evoked responses. When astrocytes are voltage-clamped near resting membrane voltage and [K$^+$]$_o$ is increased, the resulting difference in reversal potential for K$^+$ leads to a change in driving force and induces an inward K$^+$ current. Three different methods for evoking changes in [K$^+$]$_o$ were used: (1) single-pulse stimulation of the PP evoking neuronal activity and subsequently causing K$^+$ release into the extracellular space; (2) direct pressure application of enhanced [K$^+$]$_o$ using a microinjection dispense system, and (3) 100 Hz PP stimulation to induce large increases in [K$^+$]$_o$. In voltage-clamped astrocytes, increases in [K$^+$]$_o$ provoked inward currents (Figure 7a) which were unaffected by glutamate transporters (as observed by adding 100 nM of the blocker TFB-TBOA; data not shown). All astrocytes showed inward currents in response to single PP stimulation (WT, 0.30 ± 0.05 pA/pF; proximal, 0.32 ± 0.05 pA/pF; distal, 0.25 ± 0.04 pA/pF). Using the Goldmann–Hodgkin–Katz equation the estimated increase in [K$^+$]$_o$ after single PP stimulation was approximately 10–14 μM. These estimated increases were variable and not significantly different between groups (Figure 7a; Kruskal–Wallis, Dunn's: WT ($n = 27$, $N = 10$) versus proximal ($n = 18$, $N = 10$), $p > 0.9999$; WT versus distal ($n = 15$, $N = 9$), $p = 0.9999$; proximal versus distal ($p = 0.9999$). Pressure application from a pipette, containing aCSF in which the [K$^+$] was enhanced to 10 mM by replacing Na$^+$ with K$^+$, positioned in the vicinity of the patched astrocyte also induced an inward K$^+$ current (Figure 7b). The variability of the

FIGURE 7 Induced inward current and membrane depolarization in response to electrical stimulation and pressure application of K$^+$ is not altered in APP/PS1 astrocytes. (a) Maximal inward current evoked upon stimulation of the PP recorded in whole-cell patched astrocytes 100 ms after stimulation in the DG and normalized for cell capacitance. Inward current amplitudes normalized for cell capacitance were comparable between all groups. (b) Peak inward currents were recorded in whole-cell patched astrocytes after local pressure application of 10 mM KCl and normalized for cell capacitance. The puff pipette was placed approximately 30 μm distant from the patched astrocyte. No significant differences are seen between WT and APP/PS1 groups. (c) PP stimulation (schematic) resulted in membrane depolarizations in whole-cell patched astrocytes in current-clamp and reflected changes in local field potentials (seen as fast peak on inset trace). Depolarization as a result of enhanced [K$^+$]$_o$ was determined 50 ms post stimulus. Membrane depolarization was similar in all groups
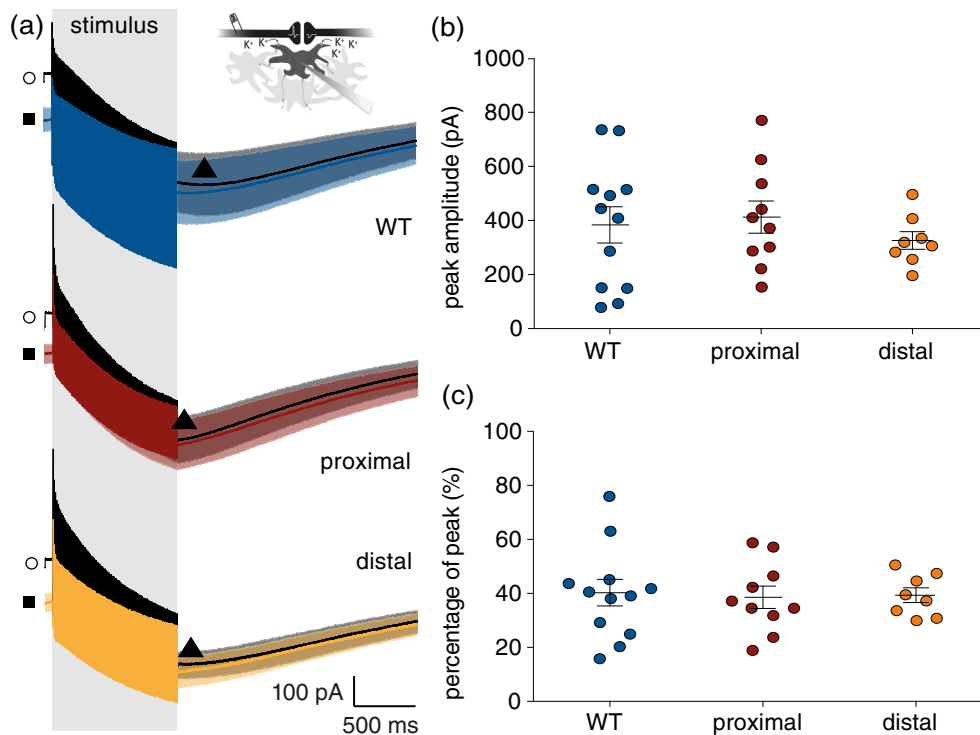
FIGURE 8 Tetanus stimulation of the PP leads to increased $[K^+]_o$ and indicates maintenance of buffering efficiency in astrocytes of APP/PS1 mice. (a) Traces are responses recorded after two 100 Hz stimuli (gray shaded band) given 6 s apart with the dark traces representing baseline (○) and initial stimulus for WT, proximal and distal astrocytes. The peak at baseline prior to the second stimulus and the response after the second tetanus are represented by the black triangle and the colored traces respectively (WT, blue; proximal, red; distal, orange). Scale is the same for all traces (100 pA and 500 ms). (b) The amplitude of the inward current, reached after the first stimulus (black triangle) appeared on average to be similar between distal, proximal, and WT astrocytes. (c) The percentage of the residual current is determined from calculating the percentage of current remaining 5 s after the first stimulus and just before giving the second stimulus (■ − ○/▲ × 100) and is not different between groups

induced currents was large (WT, 21–499 pA; proximal, 122–381 pA; distal, 57–233 pA) and not significantly different between groups after normalization to cell capacitance (Figure 7b; WT: 10.8 ± 2.3 pA/pF, proximal: 10.0 ± 2.6 pA/pF, distal: 5.6 ± 1.0 pA/pF; Kruskal–Wallis, Dunn's: WT ($n = 17$, $N = 7$) versus proximal ($n = 9$, $N = 8$), $p > 0.9999$; WT versus distal ($n = 8$, $N = 6$), $p > 0.9999$; proximal versus distal ($p > 0.9999$). Local field potential recordings via the astrocyte patch pipette (afEPSP) are possible because of the low membrane resistance of astrocytes (Henneberger & Rusakov, 2012). This approach is used to simultaneously record the afEPSP and the astrocyte depolarization. $[K^+]_o$-increase induced depolarizations were recorded in current-clamp and taken 50 ms after PP stimulation (Figure 7c). Current clamp recordings were discarded if the form of the afEPSP was distorted by the population spike or showed form variation that compromised the peak detection. The estimated membrane depolarizations resulting from a $[K^+]_o$ increase in the proximal and distal astrocytes were not significantly different (Figure 7c; WT: 0.15 ± 0.02 mV, proximal: 0.20 ± 0.02 mV, distal: 0.13 ± 0.02 mV; Kruskal–Wallis, Dunn's: WT ($n = 32$, $N = 14$) vs. proximal ($n = 18$, $N = 14$), $p = 0.3672$; WT versus distal ($n = 17$, $N = 12$), $p > 0.9999$; proximal versus distal ($p = 0.1412$). Using the Goldman-Hodgkin–Katz equation an estimated increase of 37–56 μM in $[K^+]_o$ led to the membrane depolarizations reported above.

3.6 | The buffering capacity of astrocytes and basic features of glutamatergic transmission remain unaltered in the DG MML and GCL of 9 M APP/PS1 mice

An important function of astrocytes is clearance of activity-dependent $[K^+]_o$ increases. As explained above, membrane currents in voltage-clamped astrocytes reflect changes in $[K^+]_o$ and can thus be used to monitor neuronal activity. To initiate a substantial increase in $[K^+]_o$ that activates K^+ clearance mechanisms, we challenged the DG with repetitive PP stimulation. Two 1 s, 100 Hz tetani were given 6 s apart while the patched astrocyte was clamped close to the resting membrane voltage ($\sim$ −80 mV). During the stimulation, astrocyte K^+ currents increased in line with the accumulation of K^+ in the extracellular space; followed by an almost exponential decay reflecting K^+ clearance. We quantified the decay after a fixed time period of 5 s after the first stimulus as a first estimate of the time constant of K^+ clearance (Figure 8a). The peak amplitude that was reached at the end of the first tetanic stimulation was similar in all groups (Figure 8b; WT: 384 ± 67 pA, proximal: 413 ± 60 pA, distal: 326 ± 33 pA; one-way ANOVA, Bonferroni's: WT ($n = 12$, $N = 4$) versus proximal ($n = 10$, $N = 3$), $p > 0.9999$; WT versus distal ($n = 8$, $N = 3$), $p > 0.9999$; proximal versus distal ($p > 0.9999$). Normalization to cell capacitance did not change this conclusion (WT: 8.9
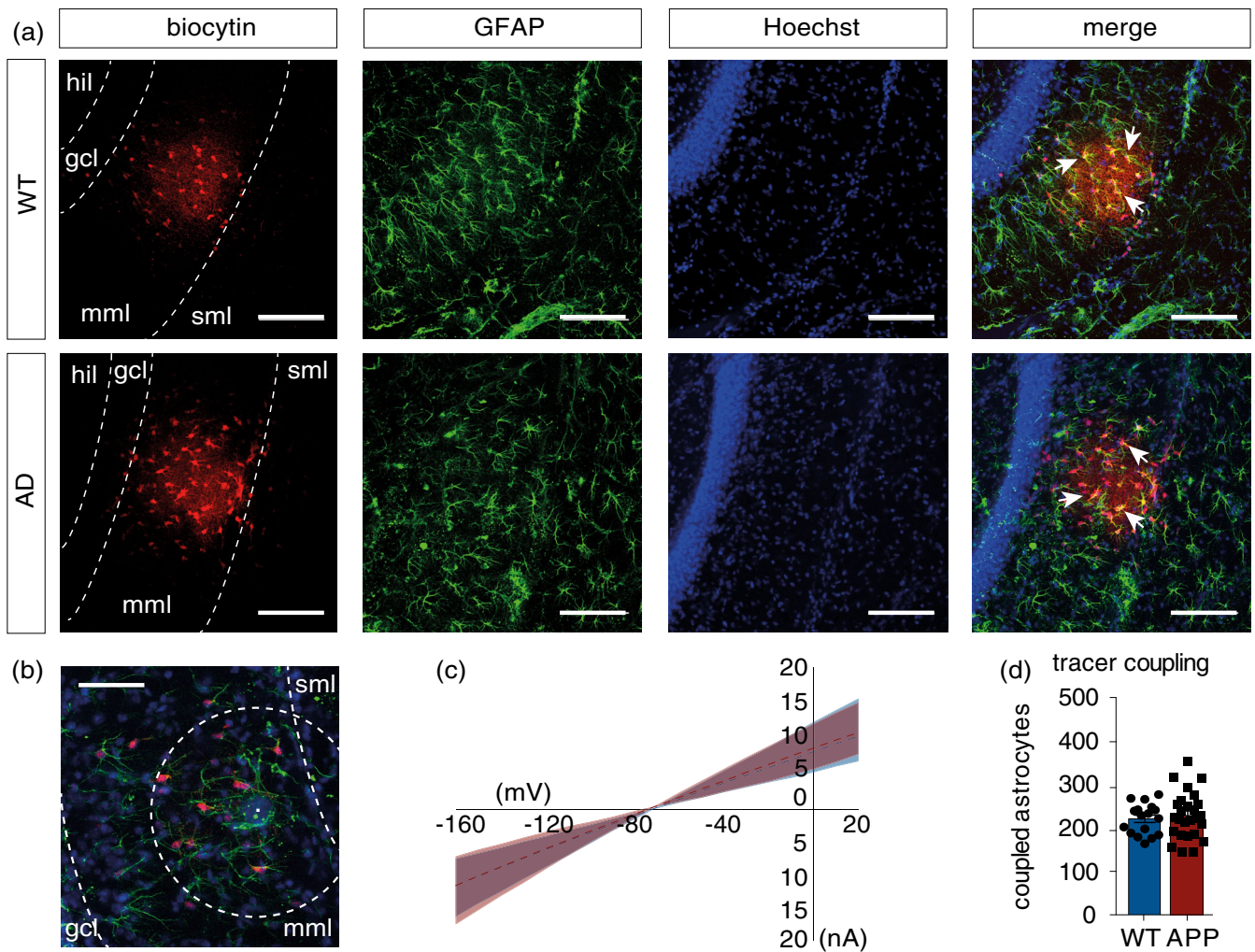
FIGURE 9 Gap junction coupling efficiency of astrocytes in the DG of 9 M APP/PS1 mice are unaltered. (a) Gap junction coupling between DG MML astrocytes in 9 M APP/PS1 mice and WT littermates. Tracer diffusion was visualized by filling an individual cell with biocytin through the patch pipette for 20 min, allowing for the diffusion of biocytin through neighboring cells in the syncytium. Subsequent immunostaining was performed to allow quantification of tracer-coupled astrocytes using a streptavidin-conjugated Alexa594 antibody. Additional staining was performed to facilitate counting using GFAP (green) and Hoechst (blue). White arrows point to biocytin$^+$/GFAP$^+$/Hoechst$^+$ cells. Scale bar: 100 μm. (b) Visual analysis of biocytin$^+$/GFAP$^+$ cells (red-biocytin; green-GFAP; blue-Hoechst) shows that astrocytes proximal to Aβ plaques (distance <80 μm) are part of the astrocyte coupling cloud. The Aβ plaque was identified in the Hoechst channel and the center is indicated by the white dot. The dashed circle indicates the 80-μm perimeter. Scale bar: 50 μm (c) The IV relation of patched astrocytes reveals a passive membrane conductance in both experimental conditions. Dashed lines represent mean values, shaded areas represent the spread of individual data points. (d) Direct comparison of the number of biocytin$^+$/GFAP$^+$ astrocytes revealed no differences in astrocyte tracer coupling efficiency between 9 M APP/PS1 mice and WT littermates

± 1.7 pA/pF, proximal: 11.6 ± 1.4 pA/pF, distal: 14.9 ± 2.2 pA/pF). In the 5 s following stimulation the current declined to 40.3 ± 4.9% for WT astrocytes, 38.6 ± 4.1% for proximal astrocytes, and 39.3 ± 2.7% for distal astrocytes (Figure 8c). These numbers were not significantly different (one-way ANOVA, Bonferroni's: WT ($n = 12$, $N = 4$) versus proximal ($n = 10$, $N = 3$), $p > 0.9999$; WT versus distal ($n = 8$, $N = 3$), $p > 0.9999$; proximal versus distal ($p > 0.9999$); K$^+$ clearance in the three groups was similar, suggesting that the K$^+$ buffering capacity of astrocytes is unaffected by the locally increased expression of Kir4.1 protein present at this stage of pathology.

To further validate this statement, we assessed whether the gap junction coupling efficiency between APP/PS1 and WT astrocytes

was altered since this directly affects the K$^+$ buffering capacity of astrocytes (Wallraff et al., 2006). This was achieved by targeting and filling a single astrocyte per brain slice with biocytin, as previously described (Wallraff et al., 2004, 2006). The subsequent staining for nuclei, GFAP, and biocytin allowed for the visualization of GFAP$^+$/biocytin$^+$ cells, and thus quantification of tracer coupled astrocytes (Figure 9a). The data showed that the number of GFAP$^+$/biocytin$^+$ cells is unaltered in APP/PS1 mice compared to littermate controls (Figure 9d; WT: 220.9 ± 8.6; APP/PS1: 228.7 ± 10.5; unpaired two-tailed t-test: WT ($n = 17$, $N = 4$) versus APP/PS1 ($n = 26$, $N = 6$), $p = 0.5995$). In addition, visual analysis showed that also astrocytes proximal to Aβ plaques (<80 μm) maintain their ability to form
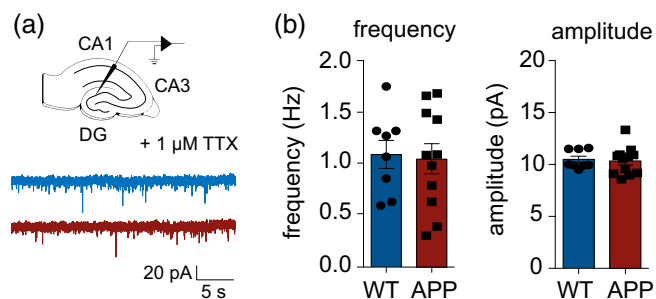
FIGURE 10 Basic features of glutamatergic transmission in the DG of 9 M APP/PS1 mice are unaltered. (a) Experimental approach and example traces. DG GCL neurons were patched in whole-cell voltage clamp configuration in the presence of 1 μM TTX to record mEPSCs. Example traces for 9 M WT and APP/PS1 are shown in blue and red, respectively. (b) Comparison of mEPSC frequency and amplitude revealed no difference between 9 M APP/PS1 mice and WT littermates

functional gap junction-coupled networks (Figure 9b). Thus, the gap junction coupling efficiency of astrocytes in the DG MML of 9 M APP/PS1 mice is not significantly different from WT conditions, further suggesting that local increases of Kir4.1 protein do not cause alterations in the K^+ buffering capacity of astrocytes.

Increases in $[K^+]_o$ and dysfunction of astrocyte Kir4.1 channels are associated with impaired glutamatergic transmission in neurons (Djukic et al., 2007; Rimmele et al., 2017). To see whether the maintained buffering capacity of astrocytes exposed to Aβ plaques is associated with intact glutamatergic transmission, we recorded mEPSCs from neurons located in the GCL of the DG (Figure 10a). Basic features of glutamatergic transmission in the GCL of the DG in 9 M APP/PS1 mice remained unchanged, as both the frequency (WT: 1.09 ± 0.14 Hz, APP/PS1: 1.05 ± 0.15 Hz; unpaired two-tailed t-test: WT ($n = 8$, $N = 4$) versus APP/PS1 ($n = 12$, $N = 5$), $p = 0.8426$) and amplitude (WT: 10.42 ± 0.31 pA; APP/PS1: 10.28 ± 0.38 pA; unpaired two-tailed t-test: WT ($n = 8$, $N = 4$) versus APP/PS1 ($n = 12$, $N = 5$), $p = 0.7918$) of recorded mEPSCs were not different between APP/PS1 and WT mice (Figure 10b).

Taken together, the results presented in this study indicate that astrocytes in 9 M APP/PS1 mice are characterized by a local increase of Kir4.1 protein expression near Aβ plaques but that this has no consequences for the K^+ buffering capacity of astrocytes, nor for basic features of glutamatergic transmission in the GCL of the DG.

4 | DISCUSSION

In many diseases, astrocytes become reactive, yet the consequences of this reactive state on cell function are unclear. The exact type of cellular reactivity and the consequences for brain function are likely to be disease-specific (Escartin et al., 2021; Pekny et al., 2016). AD is a highly prevalent disease characterized by high levels of reactive gliosis, but little is known about the role gliosis plays in this disease. To adequately assess AD pathogenesis in light of the essential role

astrocytes play in healthy brain functioning, it is key to understand how astrocytes contribute to the disease process. In this study, we show that astrocytes undergo cytoskeletal changes in response to Aβ plaque pathology in the DG MML of 9 M APP/PS1 mice, suggesting a reactive state. Earlier published transcriptomics data suggest that reactive astrocytes in AD progression are characterized by differentially expressed genes involved in the regulation of synaptic transmission and ion homeostasis (Orre, Kamphuis, Osborn, Melief, et al., 2014). Given that the inward rectifying K^+ channel Kir4.1 is particularly important for the regulation of ion homeostasis by astrocytes, we studied its expression and localization and assessed functional changes related to Kir4.1 channel expression by patch-clamp recordings from astrocytes proximal and distal to Aβ plaques. Our findings demonstrate that despite significant changes in local Kir4.1 protein expression, no changes in astroglial Kir current are present. Additionally, analysis of the astrocyte gap junction coupling efficiency by tracer diffusion shows that gap junction coupling remains intact in reactive astrocytes. Together with the results from experiments challenging the astrocyte network with increases in $[K^+]_o$ our findings suggest that K^+ clearance is similar between APP/PS1 and WT astrocytes at this stage in disease progression. Indeed, in human AD post-mortem brain material no change in $[K^+]_o$ was observed (Graham et al., 2015), which corroborates our data.

Our immunohistochemical stainings revealed an upregulation of Kir4.1 in $GFAP^+$ astrocytes adjacent to Aβ plaques. The upregulation of Kir4.1 protein is present in both the cortex and the hippocampus, and appears to be plaque-dependent in both 9 M and 15 M mice. At 9 M, the pattern of increased Kir4.1 expression is most obvious in the DG in comparison to the cortex. The local upregulation of Kir4.1 protein is unexpected as it was previously found that Kir4.1 mRNA and protein levels are reduced in AD mice (Wilcock et al., 2009). It is important, however, to realize that the upregulation of Kir4.1 expression is relative to Kir4.1 expression >80 μm from the center of the plaque. As Kir4.1 immunofluorescence was quantified relative to the mean background immunofluorescence, we can currently not draw any conclusions on how Kir4.1 expression levels in the DG MML of 9 M APP/PS1 mice compare to physiological conditions. Furthermore, differences between AD mouse models may underlie these contrasting observations as a reduction of Kir4.1 mRNA and protein was only apparent in the severe APPSwDI mouse model. APPSw mice, on the other hand, develop a mild AD phenotype and showed no clear reduction in Kir4.1 mRNA and protein expression (Wilcock et al., 2009). Likewise, our analysis on MAC-sorted hippocampal and cortical astrocytes revealed no difference in Kir4.1 mRNA expression. Discrepancies between Kir4.1 protein and mRNA expression have been reported previously (Nakajima et al., 2013). This apparent contradiction suggests that Kir4.1 protein levels increase via mechanisms other than enhanced gene transcription. These include altered translational processes or post-translational modifications, and reduced Kir4.1 protein degradation due to decreased proteasome function. Especially proteasome dysfunction has been implicated in multiple neurodegenerative diseases, including AD (Bonet-Costa et al., 2016). This, combined with APP/PS1 models reflecting disease-related

symptoms differently, probably contributes to the opposing findings reported in literature with respect to Kir4.1 mRNA and protein levels.

Though staining of Kir4.1 is also visible in non-plaque associated areas, it is difficult to ascertain potential quantitative changes in Kir4.1 in non-plaque associated astrocytes using immunohistochemistry. It was however apparent that increases in Kir4.1 expression were heterogeneous overall since not all GFAP$^+$ astrocytes proximal to Aβ plaques showed the same levels of increased Kir4.1 expression. The heterogeneous character of Kir4.1 expression could be due to Kir4.1 also being increasingly expressed by other cell types. Kir4.1 is expressed in NG2 glial cells displaying complex current patterns (Hsu et al., 2011; Schröder et al., 2002; Steinhäuser et al., 1994; Tang et al., 2009). Additionally, Kir4.1 is present in Olig2$^+$ cells of the hippocampus and cortex, however in far lower concentrations than found in astrocytes (Moroni et al., 2015). Indeed, additional analysis revealed that Kir4.1 fluorescence only rarely co-localized with Olig2$^+$ cells. Our confocal images also show clear co-localization of Kir4.1 with GFAP, underscoring its presence in astrocytes and suggesting an upregulation of Kir4.1 protein in areas with high plaque burden.

Despite this difference in Kir4.1 protein distribution, we found no evidence of changes in passive membrane properties between WT and APP/PS1 astrocytes. Both in APP/PS1 and WT conditions a low membrane resistance, negative resting membrane potential, and a large K$^+$-conductance are key characteristics of these cells. We also found no changes in passive current profiles. This finding contrasts to observations made in other diseases such as temporal lobe epilepsy (Bedner et al., 2015) and stab-wound injury (Sirko et al., 2013), where the current profiles of reactive astrocytes are no longer dominated by a passive K$^+$ conductance. Although recordings were obtained from presumed reactive astrocytes, our results also indicate that astrocytes in APP/PS1 mice maintain their gap junction coupling efficiency, which could partially account for the apparent absence of differences in electrophysiological properties. Additionally, our findings do not exclude potential changes in the composition of the Kir conductance observed in these cells. Astrocytes express homomeric Kir4.1 channels but also heteromeric co-assemblies between Kir4.1 and other subtypes, such as Kir2 family members or Kir5.1 (Butt & Kalsi, 2006; Schröder et al., 2002). These Kir co-assemblies all differ in their biophysical properties and changes in the expression of individual channel types might compensate for each other so that the overall current pattern and membrane properties remain similar. Altogether, this points to reactive gliosis as a heterogeneous response instead of a universal principle, that is dependent on the environment and the specific pathological process (Sofroniew, 2009).

To make the comparison between astrocytes proximal and distal to Aβ plaques, we used 9 M APP/PS1 mice. When older, the plaque density within the DG is too high, which makes such a comparison impossible (Jankowsky et al., 2004). Subdividing APP/PS1 astrocytes into proximal ($\leq$80 μm distant to an Aβ plaque) and distal (>100 μm distant to Aβ plaque) groups did not reveal any differences in general electrophysiological properties nor Kir4.1 functionality. This was contrary to our expectations since astrocytes <80 μm away from an Aβ plaque undergo distinct phenotypic and morphological changes, such as

hypertrophy and increased GFAP expression, both classical markers of gliosis present in the hippocampus (Bouvier et al., 2016; Galea et al., 2015; Serrano-Pozo et al., 2013). Changes in more distal astrocytes, however, are less well defined. Indeed, our immunostainings showed that astrocytes characterized by cytoskeletal alterations are more likely to be located adjacent to Aβ plaques in the DG MML. Nevertheless, basic membrane properties and the proportion of Ba^{2+}-sensitive currents remained unchanged in proximal versus distal astrocytes. However, a caveat in ascertaining proximity to an Aβ plaque ex-vivo is that the slice preparation removes cells from their three-dimensional surroundings and may therefore falsely categorize astrocytes as distal. This is a potential source of variability within the APP/PS1 group. Additionally, the gap junction coupling and low input resistance of astrocytes in situ significantly impair temporal and spatial clamp conditions and hence affect quantitative functional analyses (Ma et al., 2014; Seifert et al., 2009, 2018). In addition, the density of Kir4.1 expression is enriched in distal processes of adult astrocytes (Higashi et al., 2001; Moroni et al., 2015) which, due to suboptimal space-clamp conditions, escape control during patch-clamp recordings. This potentially explains why the recorded proportion of Ba^{2+}-sensitive currents was relatively small. Use of astrocytes freshly isolated from the tissue (Seifert et al., 2009) and utilizing mice with genetically uncoupled astrocytes (by crossing the APP/PS1 mouse with Cx30$^{-/-}$, Cx43$^{fl/fl}$ GFAP: Cre mice; (Wallraff et al., 2006) would help improve space-clamp conditions.

Together, our functional data suggest that the buffering capacity for K$^+$ is robust and unchanged in astrocytes of 9 M APP/PS1 mice. Both the percentage of inward current remaining after tetanic stimulation and the time constant for relaxation of the current back to baseline suggests that the ability to dissipate increased [K$^+$]$_o$ does not differ between WT and APP/PS1 astrocytes. This possibility is further endorsed by our finding that gap junction coupling between astrocytes is not affected at this age in our model. Accordingly, where increases in [K$^+$]$_o$ and dysfunction of astrocyte Kir4.1 channels are associated with impaired glutamatergic transmission in neurons (Djukic et al., 2007; Rimmele et al., 2017), our data indicate that basic features of glutamatergic transmission remain unchanged in the GCL of the DG in 9 M APP/PS1 mice.

Although we recorded both from proximal and distal astrocytes, it has to be taken into account that astrocytes within the DG are not homogeneous in their response to pathology. It is clear from the literature, as well as our data, that astrocytes surrounding Aβ plaques in various brain areas of AD mouse models, including the DG, are hypertrophic and increase GFAP expression (Girard et al., 2014; Kamphuis et al., 2012; Norris et al., 2005; Olabarria et al., 2010). Yet, these classical markers for astrogliosis seem to be absent in non-plaque associated astrocytes. This population may however represent a different class of reactive astrocytes. In fact, one study of PDAPP-J20 mice showed decreased cell volume and increased process complexity in non-plaque associated astrocytes when compared to WT littermates; these alterations were also evidently different to plaque-associated astrocytes (Beaquis et al., 2013). These changes are perhaps indicative of multi-stage and milieu-dependent reactivity that may also

depend on the presence and concentration of oligomeric Aβ. Other studies of a triple-transgenic mouse model of AD found the presence of astrocyte atrophy preceding plaque deposition (Kulijewicz-Nawrot et al., 2012; Olabarria et al., 2010; Yeh et al., 2011).

In conclusion, astrocytes within the DG are heterogeneous with respect to their reactive phenotype and Kir conductance. Our research shows that Kir4.1 protein expression is upregulated in plaque-associated astrocytes. These astrocytes, however, maintain their ability to clear K^+ despite AD pathology and Kir channel dysfunction is likely not attributable to plaque deposition.

DATA AVAILABILITY STATEMENT

All data are available upon request to e.m.hol-2@umcutrecht.nl.

ORCID

Christiaan F. M. Huffels https://orcid.org/0000-0002-9070-3644
Lana M. Osborn https://orcid.org/0000-0002-5900-0246
Lianne A. Hulshof https://orcid.org/0000-0002-6227-4336
Christian Steinhäuser https://orcid.org/0000-0003-2579-8357
Elly M. Hol https://orcid.org/0000-0001-5604-2603

REFERENCES

Akopian, G., Kuprijanova, E., Kressin, K., & Steinhäuser, C. (1997). Analysis of ion channel expression by astrocytes in red nucleus brain stem slices of the rat. *Glia*, *19*(3), 234–246.

Beauquis, J., Pavía, P., Pomilio, C., Vinuesa, A., Podlutskaya, N., Galvan, V., & Saravia, F. (2013). Environmental enrichment prevents astroglial pathological changes in the hippocampus of APP transgenic mice, model of Alzheimer's disease. *Experimental Neurology*, *239*, 28–37. https://doi.org/10.1016/j.expneurol.2012.09.009

Bedner, P., Dupper, A., Hüttmann, K., Müller, J., Herde, M. K., Dublin, P., Deshpande, T., Schramm, J., Häussler, U., Haas, C. A., Henneberger, C., Theis, M., & Steinhäuser, C. (2015). Astrocyte uncoupling as a cause of human temporal lobe epilepsy. *Brain*, *138*(5), 1208–1222. https://doi.org/10.1093/brain/awv067

Bedner, P., & Steinhäuser, C. (2013). Altered Kir and gap junction channels in temporal lobe epilepsy. *Neurochemistry International*, *63*(7), 682–687. https://doi.org/10.1016/j.neuint.2013.01.011

Bonet-Costa, V., Pomatto, L. C.-D., & Davies, K. J. A. (2016). The proteasome and oxidative stress in Alzheimer's disease. *Antioxidants & Redox Signaling*, *25*(16), 886–901. https://doi.org/10.1089/ars.2016.6802

Bossers, K., Wirz, K. T. S., Meerhoff, G. F., Essing, A. H. W., van Dongen, J. W., Houba, P., Kruse, C. G., Verhaagen, J., & Swaab, D. F. (2010). Concerted changes in transcripts in the prefrontal cortex precede neuropathology in Alzheimer's disease. *Brain*, *133*(Pt 12), 3699–3723. https://doi.org/10.1093/brain/awq258

Bouvier, D. S., Jones, E. V., Quesseveur, G., Davoli, M. A., Ferreira, A., Quirion, R., Mechawar, N., & Murai, K. K. (2016). High resolution dissection of reactive glial nets in Alzheimer's disease. *Scientific Reports*, *6*, 24544. https://doi.org/10.1038/srep24544

Bushong, E. A., Martone, M. E., Jones, Y. Z., & Ellisman, M. H. (2002). Protoplasmic astrocytes in CA1 stratum radiatum occupy separate anatomical domains. *The Journal of Neuroscience*, *22*(1), 183–192. https://doi.org/10.1523/JNEUROSCI.22-01-00183.2002

Butt, A. M., & Kalsi, A. (2006). Inwardly rectifying potassium channels (Kir) in central nervous system glia: A special role for Kir4.1 in glial functions. *Journal of Cellular and Molecular Medicine*, *10*(1), 33–44. https://doi.org/10.1111/j.1582-4934.2006.tb00289.x

Coetzee, W. A., Amarillo, Y., Chiu, J., Chow, A., Lau, D., McCormack, T., Moreno, H., Nadal, M. S., Ozaita, A., Pountney, D., Saganich, M., Vega-Saenz de Miera, E., & Rudy, B. (1999). Molecular diversity of K+ channels. *Annals of the New York Academy of Sciences*, *868*, 233–285. https://doi.org/10.1111/j.1749-6632.1999.tb11293.x

Corbett, B. F., Leiser, S. C., Ling, H.-P., Nagy, R., Breysse, N., Zhang, X., Hazra, A., Brown, J. T., Randall, A. D., Wood, A., Pangalos, M. N., Reinhart, P. H., & Chin, J. (2013). Sodium channel cleavage is associated with aberrant neuronal activity and cognitive deficits in a mouse model of Alzheimer's disease. *The Journal of Neuroscience*, *33*(16), 7020–7026. https://doi.org/10.1523/JNEUROSCI.2325-12.2013

Dai, A. I., Akcali, A., Koska, S., Oztuzcu, S., Cengiz, B., & Demiryürek, A. T. (2015). Contribution of KCNJ10 gene polymorphisms in childhood epilepsy. *Journal of Child Neurology*, *30*(3), 296–300. https://doi.org/10.1177/0883073814539560

Del Vecchio, R. A., Gold, L. H., Novick, S. J., Wong, G., & Hyde, L. A. (2004). Increased seizure threshold and severity in young transgenic CRND8 mice. *Neuroscience Letters*, *367*(2), 164–167. https://doi.org/10.1016/j.neulet.2004.05.107

Delekate, A., Füchtemeier, M., Schumacher, T., Ulbrich, C., Foddis, M., & Petzold, G. C. (2014). Metabotropic P2Y1 receptor signalling mediates astrocytic hyperactivity in vivo in an Alzheimer's disease mouse model. *Nature Communications*, *5*, 5422. https://doi.org/10.1038/ncomms6422

Djukic, B., Casper, K. B., Philpot, B. D., Chin, L.-S., & McCarthy, K. D. (2007). Conditional Knock-out of Kir4.1 leads to glial membrane depolarization, inhibition of potassium and glutamate uptake, and enhanced short-term synaptic potentiation. *Journal of Neuroscience*, *27*(42), 11354–11365. https://doi.org/10.1523/JNEUROSCI.0723-07.2007

Escartin, C., Galea, E., Lakatos, A., O'Callaghan, J. P., Petzold, G. C., Serrano-Pozo, A., Steinhäuser, C., Volterra, A., Carmignoto, G., Agarwal, A., Allen, N. J., Araque, A., Barbeito, L., Barzilai, A., Bergles, D. E., Bonvento, G., Butt, A. M., Chen, W.-T., Cohen-Salmon, M., ... Verkhratsky, A. (2021). Reactive astrocyte nomenclature, definitions, and future directions. *Nature Neuroscience*, *24*(3), 312–325. https://doi.org/10.1038/s41593-020-00783-4

Ferraro, T. N., Golden, G. T., Smith, G. G., Martin, J. F., Lohoff, F. W., Gieringer, T. A., Zamboni, D., Schwebel, C. L., Press, D. M., Kratzer, S. O., Zhao, H., Berrettini, W. H., & Buono, R. J. (2004). Fine mapping of a seizure susceptibility locus on mouse chromosome 1: Nomination of Kcnj10 as a causative gene. *Mammalian Genome*, *15*(4), 239–251. https://doi.org/10.1007/s00335-003-2270-3

Galea, E., Morrison, W., Hudry, E., Arbel-Ornath, M., Bacskai, B. J., Gómez-Isla, T., Stanley, H. E., & Hyman, B. T. (2015). Topological analyses in APP/PS1 mice reveal that astrocytes do not migrate to amyloid-β plaques. *Proceedings of the National Academy of Sciences of the United States of America*, *112*(51), 15556–15561. https://doi.org/10.1073/pnas.1516779112

Girard, S. D., Jacquet, M., Baranger, K., Migliorati, M., Escoffier, G., Bernard, A., Khrestchatisky, M., Féron, F., Rivera, S., Roman, F. S., & Marchetti, E. (2014). Onset of hippocampus-dependent memory impairments in 5XFAD transgenic mouse model of Alzheimer's disease. *Hippocampus*, *24*(7), 762–772. https://doi.org/10.1002/hipo.22267

Graham, S. F., Nasaruddin, M. B., Carey, M., McGuinness, B., Holscher, C., Kehoe, P. G., Love, S., Passmore, A. P., Elliott, C. T., Meharg, A., &

Green, B. D. (2015). Quantitative measurement of [Na+] and [K+] in post-mortem human brain tissue indicates disturbances in subjects with Alzheimer's disease and dementia with Lewy bodies. *Journal of Alzheimer's Disease*, 44(3), 851–857. https://doi.org/10.3233/JAD-141869

Gurevicius, K., Lipponen, A., & Tanila, H. (2013). Increased cortical and thalamic excitability in freely moving APPswe/PS1dE9 mice modeling epileptic activity associated with Alzheimer's disease. *Cerebral Cortex*, 23(5), 1148–1158. https://doi.org/10.1093/cercor/bhs105

Hazra, A., Corbett, B. F., You, J. C., Aschmies, S., Zhao, L., Li, K., Lepore, A. C., Marsh, E. D., & Chin, J. (2016). Corticothalamic network dysfunction and behavioral deficits in a mouse model of Alzheimer's disease. *Neurobiology of Aging*, 44, 96–107. https://doi.org/10.1016/j.neurobiolaging.2016.04.016

Henneberger, C., & Rusakov, D. A. (2012). Monitoring local synaptic activity with astrocytic patch pipettes. *Nature Protocols*, 7(12), 2171–2179. https://doi.org/10.1038/nprot.2012.140

Higashi, K., Fujita, A., Inanobe, A., Tanemoto, M., Doi, K., Kubo, T., & Kurachi, Y. (2001). An inwardly rectifying K(+) channel, Kir4.1, expressed in astrocytes surrounds synapses and blood vessels in brain. *American Journal of Physiology. Cell Physiology*, 281(3), C922–C931. https://doi.org/10.1152/ajpcell.2001.281.3.C922

Hol, E. M., & Pekny, M. (2015). Glial fibrillary acidic protein (GFAP) and the astrocyte intermediate filament system in diseases of the central nervous system. *Current Opinion in Cell Biology*, 32, 121–130. https://doi.org/10.1016/j.ceb.2015.02.004

Hsu, M. S., Seldin, M., Lee, D. J., Seifert, G., Steinhäuser, C., & Binder, D. K. (2011). Laminar-specific and developmental expression of aquaporin-4 in the mouse hippocampus. *Neuroscience*, 178, 21–32. https://doi.org/10.1016/j.neuroscience.2011.01.020

Jacob, C. P., Koutsilieri, E., Bartl, J., Neuen-Jacob, E., Arzberger, T., Zander, N., Ravid, R., Roggendorf, W., Riederer, P., & Grünblatt, E. (2007). Alterations in expression of glutamatergic transporters and receptors in sporadic Alzheimer's disease. *Journal of Alzheimer's Disease*, 11(1), 97–116. https://doi.org/10.3233/jad-2007-11113

Jankowsky, J. L., Fadale, D. J., Anderson, J., Xu, G. M., Gonzales, V., Jenkins, N. A., Copeland, N. G., Lee, M. K., Younkin, L. H., Wagner, S. L., Younkin, S. G., & Borchelt, D. R. (2004). Mutant presenilins specifically elevate the levels of the 42 residue beta-amyloid peptide in vivo: Evidence for augmentation of a 42-specific gamma secretase. *Human Molecular Genetics*, 13(2), 159–170. https://doi.org/10.1093/hmg/ddh019

Jo, S., Yarishkin, O., Hwang, Y. J., Chun, Y. E., Park, M., Woo, D. H., Bae, J. Y., Kim, T., Lee, J., Chun, H., Park, H. J., Da Yong, L., Hong, J., Kim, H. Y., Oh, S.-J., Park, S. J., Lee, H., Yoon, B.-E., Kim, Y., ... Lee, C. J. (2014). GABA from reactive astrocytes impairs memory in mouse models of Alzheimer's disease. *Nature Medicine*, 20(8), 886–896. https://doi.org/10.1038/nm.3639

Kamphuis, W., Mamber, C., Moeton, M., Kooijman, L., Sluijs, J. A., Jansen, A. H. P., Verveer, M., de Groot, L. R., Smith, V. D., Rangarajan, S., Rodríguez, J. J., Orre, M., & Hol, E. M. (2012). GFAP isoforms in adult mouse brain with a focus on neurogenic astrocytes and reactive astrogliosis in mouse models of Alzheimer disease. *PLoS One*, 7(8), e42823. https://doi.org/10.1371/journal.pone.0042823

Kamphuis, W., Middeldorp, J., Kooijman, L., Sluijs, J. A., Kooi, E.-J., Moeton, M., Freriks, M., Mizee, M. R., & Hol, E. M. (2014). Glial fibrillary acidic protein isoform expression in plaque related astrogliosis in Alzheimer's disease. *Neurobiology of Aging*, 35(3), 492–510. https://doi.org/10.1016/j.neurobiolaging.2013.09.035

Klunk, W. E., Bacskai, B. J., Mathis, C. A., Kajdasz, S. T., McLellan, M. E., Frosch, M. P., Debnath, M. L., Holt, D. P., Wang, Y., & Hyman, B. T. (2002). Imaging Abeta plaques in living transgenic mice with multiphoton microscopy and methoxy-X04, a systemically administered Congo red derivative. *Journal of Neuropathology and Experimental Neurology*, 61(9), 797–805. https://doi.org/10.1093/jnen/61.9.797

Kuchibhotla, K. V., Lattarulo, C. R., Hyman, B. T., & Bacskai, B. J. (2009). Synchronous hyperactivity and intercellular calcium waves in astrocytes in Alzheimer mice. *Science*, 323(5918), 1211–1215. https://doi.org/10.1126/science.1169096

Kulijewicz-Nawrot, M., Verkhratsky, A., Chvátal, A., Syková, E., & Rodríguez, J. J. (2012). Astrocytic cytoskeletal atrophy in the medial prefrontal cortex of a triple transgenic mouse model of Alzheimer's disease. *Journal of Anatomy*, 221(3), 252–262. https://doi.org/10.1111/j.1469-7580.2012.01536.x

Ma, B., Xu, G., Wang, W., Enyeart, J. J., & Zhou, M. (2014). Dual patch voltage clamp study of low membrane resistance astrocytes in situ. *Molecular Brain*, 7, 18. https://doi.org/10.1186/1756-6606-7-18

Malm, T. M., Iivonen, H., Goldsteins, G., Keksa-Goldsteine, V., Ahtoniemi, T., Kanninen, K., Salminen, A., Auriola, S., Van Groen, T., Tanila, H., & Koistinaho, J. (2007). Pyrrolidine dithiocarbamate activates Akt and improves spatial learning in APP/PS1 mice without affecting beta-amyloid burden. *The Journal of Neuroscience*, 27(14), 3712–3721. https://doi.org/10.1523/JNEUROSCI.0059-07.2007

Meeker, K. D., Meabon, J. S., & Cook, D. G. (2015). Partial loss of the glutamate transporter GLT-1 alters brain Akt and insulin signaling in a mouse model of Alzheimer's disease. *Journal of Alzheimer's Disease*, 45(2), 509–520. https://doi.org/10.3233/JAD-142304

Minkeviciene, R., Rheims, S., Dobszay, M. B., Zilberter, M., Hartikainen, J., Fülöp, L., Penke, B., Zilberter, Y., Harkany, T., Pitkänen, A., & Tanila, H. (2009). Amyloid beta-induced neuronal hyperexcitability triggers progressive epilepsy. *The Journal of Neuroscience*, 29(11), 3453–3462. https://doi.org/10.1523/JNEUROSCI.5215-08.2009

Moloney, A. M., Griffin, R. J., Timmons, S., O'Connor, R., Ravid, R., & O'Neill, C. (2010). Defects in IGF-1 receptor, insulin receptor and IRS-1/2 in Alzheimer's disease indicate possible resistance to IGF-1 and insulin signalling. *Neurobiology of Aging*, 31(2), 224–243. https://doi.org/10.1016/j.neurobiolaging.2008.04.002

Moroni, R. F., Inverardi, F., Regondi, M. C., Pennacchio, P., & Frassoni, C. (2015). Developmental expression of Kir4.1 in astrocytes and oligodendrocytes of rat somatosensory cortex and hippocampus. *International Journal of Developmental Neuroscience*, 47, 198–205. https://doi.org/10.1016/j.ijdevneu.2015.09.004

Nakajima, M., Kawamura, T., Tokui, R., Furuta, K., Sugino, M., Nakanishi, M., Okuyama, S., & Furukawa, Y. (2013). Enhanced accumulation of Kir4.1 protein, but not mRNA, in a murine model of cuprizone-induced demyelination. *Brain Research*, 1537, 340–349. https://doi.org/10.1016/j.brainres.2013.09.024

Newman, E. A. (1986). High potassium conductance in astrocyte endfeet. *Science*, 233(4762), 453–454. https://doi.org/10.1126/science.3726539

Noebels, J. (2011). A perfect storm: Converging paths of epilepsy and Alzheimer's dementia intersect in the hippocampal formation. *Epilepsia*, 52(Suppl 1), 39–46. https://doi.org/10.1111/j.1528-1167.2010.02909.x

Norris, C. M., Kadish, I., Blalock, E. M., Chen, K.-C., Thibault, V., Porter, N. M., Landfield, P. W., & Kraner, S. D. (2005). Calcineurin triggers reactive/inflammatory processes in astrocytes and is upregulated in aging and Alzheimer's models. *The Journal of Neuroscience*, 25(18), 4649–4658. https://doi.org/10.1523/JNEUROSCI.0365-05.2005

Olabarria, M., Noristani, H. N., Verkhratsky, A., & Rodríguez, J. J. (2010). Concomitant astroglial atrophy and astrogliosis in a triple transgenic animal model of Alzheimer's disease. *Glia*, 58(7), 831–838. https://doi.org/10.1002/glia.20967

Orre, M., Kamphuis, W., Osborn, L. M., Jansen, A. H. P., Kooijman, L., Bossers, K., & Hol, E. M. (2014). Isolation of glia from Alzheimer's mice reveals inflammation and dysfunction. *Neurobiology of Aging*, 35(12), 2746–2760. https://doi.org/10.1016/j.neurobiolaging.2014.06.004

Orre, M., Kamphuis, W., Osborn, L. M., Melief, J., Kooijman, L., Huitinga, I., Klooster, J., Bossers, K., & Hol, E. M. (2014). Acute isolation and transcriptome characterization of cortical astrocytes and microglia from

young and aged mice. *Neurobiology of Aging*, 35(1), 1–14. https://doi.org/10.1016/j.neurobiolaging.2013.07.008

Ortinski, P. I., Dong, J., Mungenast, A., Yue, C., Takano, H., Watson, D. J., Haydon, P. G., & Coulter, D. A. (2010). Selective induction of astrocytic gliosis generates deficits in neuronal inhibition. *Nature Neuroscience*, 13(5), 584–591. https://doi.org/10.1038/nn.2535

Osborn, L. M., Kamphuis, W., Wadman, W. J., & Hol, E. M. (2016). Astrogliosis: An integral player in the pathogenesis of Alzheimer's disease. *Progress in Neurobiology*, 144, 121–141. https://doi.org/10.1016/j.pneurobio.2016.01.001

Palop, J. J., Chin, J., Roberson, E. D., Wang, J., Thwin, M. T., Bien-Ly, N., Yoo, J., Ho, K. O., Yu, G.-Q., Kreitzer, A., Finkbeiner, S., Noebels, J. L., & Mucke, L. (2007). Aberrant excitatory neuronal activity and compensatory remodeling of inhibitory hippocampal circuits in mouse models of Alzheimer's disease. *Neuron*, 55(5), 697–711. https://doi.org/10.1016/j.neuron.2007.07.025

Pekny, M., Pekna, M., Messing, A., Steinhäuser, C., Lee, J.-M., Parpura, V., Hol, E. M., Sofroniew, M. V., & Verkhratsky, A. (2016). Astrocytes: A central element in neurological diseases. *Acta Neuropathologica*, 131(3), 323–345. https://doi.org/10.1007/s00401-015-1513-1

Peters, O., Schipke, C. G., Philipps, A., Haas, B., Pannasch, U., Wang, L. P., Benedetti, B., Kingston, A. E., & Kettenmann, H. (2009). Astrocyte function is modified by Alzheimer's disease-like pathology in aged mice. *Journal of Alzheimer's Disease*, 18(1), 177–189. https://doi.org/10.3233/JAD-2009-1140

Querfurth, H. W., & LaFerla, F. M. (2010). Alzheimer's disease. *The New England Journal of Medicine*, 362(4), 329–344. https://doi.org/10.1056/NEJMra0909142

Rao, S. C., Dove, G., Cascino, G. D., & Petersen, R. C. (2009). Recurrent seizures in patients with dementia: Frequency, seizure types, and treatment outcome. *Epilepsy & Behavior*, 14(1), 118–120. https://doi.org/10.1016/j.yebeh.2008.08.012

Rimmele, T. S., Rocher, A.-B., Wellbourne-Wood, J., & Chatton, J.-Y. (2017). Control of glutamate transport by extracellular potassium: Basis for a negative feedback on synaptic transmission. *Cerebral Cortex*, 27(6), 3272–3283. https://doi.org/10.1093/cercor/bhx078

Rose, C. R., & Verkhratsky, A. (2016). Glial ionic excitability: The role for sodium: Glial ionic excitability. *Glia*, 64(10), 1609–1610. https://doi.org/10.1002/glia.23012

Schallier, A., Smolders, I., Van Dam, D., Loyens, E., De Deyn, P. P., Michotte, A., Michotte, Y., & Massie, A. (2011). Region- and age-specific changes in glutamate transport in the AβPP23 mouse model for Alzheimer's disease. *Journal of Alzheimer's Disease*, 24(2), 287–300. https://doi.org/10.3233/JAD-2011-101005

Schindelin, J., Arganda-Carreras, I., Frise, E., Kaynig, V., Longair, M., Pietzsch, T., Preibisch, S., Rueden, C., Saalfeld, S., Schmid, B., Tinevez, J.-Y., White, D. J., Hartenstein, V., Eliceiri, K., Tomancak, P., & Cardona, A. (2012). Fiji: An open-source platform for biological-image analysis. *Nature Methods*, 9(7), 676–682. https://doi.org/10.1038/nmeth.2019

Schnell, C., Shahmoradi, A., Wichert, S. P., Mayerl, S., Hagos, Y., Heuer, H., Rossner, M. J., & Hülsmann, S. (2015). The multispecific thyroid hormone transporter OATP1C1 mediates cell-specific sulforhodamine 101-labeling of hippocampal astrocytes. *Brain Structure and Function*, 220(1), 193–203. https://doi.org/10.1007/s00429-013-0645-0

Schröder, W., Seifert, G., Hüttmann, K., Hinterkeuser, S., & Steinhäuser, C. (2002). AMPA receptor-mediated modulation of inward rectifier K+ channels in astrocytes of mouse hippocampus. *Molecular and Cellular Neurosciences*, 19(3), 447–458. https://doi.org/10.1006/mcne.2001.1080

Seifert, G., Henneberger, C., & Steinhäuser, C. (2018). Diversity of astrocyte potassium channels: An update. *Brain Research Bulletin*, 136, 26–36. https://doi.org/10.1016/j.brainresbull.2016.12.002

Seifert, G., Hüttmann, K., Binder, D. K., Hartmann, C., Wyczynski, A., Neusch, C., & Steinhäuser, C. (2009). Analysis of astroglial K+ channel expression in the developing hippocampus reveals a predominant role of the Kir4.1 subunit. *The Journal of Neuroscience*, 29(23), 7474–7488. https://doi.org/10.1523/JNEUROSCI.3790-08.2009

Sekar, S., McDonald, J., Cuyugan, L., Aldrich, J., Kurdoglu, A., Adkins, J., Serrano, G., Beach, T. G., Craig, D. W., Valla, J., Reiman, E. M., & Liang, W. S. (2015). Alzheimer's disease is associated with altered expression of genes involved in immune response and mitochondrial processes in astrocytes. *Neurobiology of Aging*, 36(2), 583–591. https://doi.org/10.1016/j.neurobiolaging.2014.09.027

Serrano-Pozo, A., Muzikansky, A., Gómez-Isla, T., Growdon, J. H., Betensky, R. A., Frosch, M. P., & Hyman, B. T. (2013). Differential relationships of reactive astrocytes and microglia to fibrillar amyloid deposits in Alzheimer disease. *Journal of Neuropathology and Experimental Neurology*, 72(6), 462–471. https://doi.org/10.1097/NEN.0b013e3182933788

Sirko, S., Behrendt, G., Johansson, P. A., Tripathi, P., Costa, M., Bek, S., Heinrich, C., Tiedt, S., Colak, D., Dichgans, M., Fischer, I. R., Plesnila, N., Staufenbiel, M., Haass, C., Snapyan, M., Saghatelyan, A., Tsai, L.-H., Fischer, A., Grobe, K., ... Götz, M. (2013). Reactive glia in the injured brain acquire stem cell properties in response to sonic hedgehog. *Cell Stem Cell*, 12(4), 426–439. https://doi.org/10.1016/j.stem.2013.01.019

Sofroniew, M. V. (2009). Molecular dissection of reactive astrogliosis and glial scar formation. *Trends in Neurosciences*, 32(12), 638–647. https://doi.org/10.1016/j.tins.2009.08.002

Somjen, G. G. (1975). Electrophysiology of neuroglia. *Annual Review of Physiology*, 37, 163–190. https://doi.org/10.1146/annurev.ph.37.030175.001115

Steinhäuser, C., Jabs, R., & Kettenmann, H. (1994). Properties of GABA and glutamate responses in identified glial cells of the mouse hippocampal slice. *Hippocampus*, 4(1), 19–35. https://doi.org/10.1002/hipo.450040105

Steinhäuser, C., Seifert, G., & Bedner, P. (2012). Astrocyte dysfunction in temporal lobe epilepsy: K+ channels and gap junction coupling. *Glia*, 60(8), 1192–1202. https://doi.org/10.1002/glia.22313

Tang, X., Taniguchi, K., & Kofuji, P. (2009). Heterogeneity of Kir4.1 channel expression in glia revealed by mouse transgenesis. *Glia*, 57(16), 1706–1715. https://doi.org/10.1002/glia.20882

Tong, X., Ao, Y., Faas, G. C., Nwaobi, S. E., Xu, J., Haustein, M. D., Anderson, M. A., Mody, I., Olsen, M. L., Sofroniew, M. V., & Khakh, B. S. (2014). Astrocyte Kir4.1 ion channel deficits contribute to neuronal dysfunction in Huntington's disease model mice. *Nature Neuroscience*, 17(5), 694–703. https://doi.org/10.1038/nn.3691

Vitvitsky, V. M., Garg, S. K., Keep, R. F., Albin, R. L., & Banerjee, R. (2012). Na+ and K+ ion imbalances in Alzheimer's disease. *Biochimica et Biophysica Acta*, 1822(11), 1671–1681. https://doi.org/10.1016/j.bbadis.2012.07.004

Vossel, K. A., Beagle, A. J., Rabinovici, G. D., Shu, H., Lee, S. E., Naasan, G., Hegde, M., Cornes, S. B., Henry, M. L., Nelson, A. B., Seeley, W. W., Geschwind, M. D., Gorno-Tempini, M. L., Shih, T., Kirsch, H. E., Garcia, P. A., Miller, B. L., & Mucke, L. (2013). Seizures and epileptiform activity in the early stages of Alzheimer disease. *JAMA Neurology*, 70(9), 1158–1166. https://doi.org/10.1001/jamaneurol.2013.136

Vossel, K. A., Ranasinghe, K. G., Beagle, A. J., Mizuiri, D., Honma, S. M., Dowling, A. F., Darwish, S. M., Van Berlo, V., Barnes, D. E., Mantle, M., Karydas, A. M., Coppola, G., Roberson, E. D., Miller, B. L., Garcia, P. A., Kirsch, H. E., Mucke, L., & Nagarajan, S. S. (2016). Incidence and impact of subclinical epileptiform activity in Alzheimer's disease. *Annals of Neurology*, 80(6), 858–870. https://doi.org/10.1002/ana.24794

Wallraff, A., Köhling, R., Heinemann, U., Theis, M., Willecke, K., & Steinhäuser, C. (2006). The impact of astrocytic gap junctional coupling on potassium buffering in the hippocampus. *The Journal of Neuroscience*, 26(20), 5438–5447. https://doi.org/10.1523/JNEUROSCI.0037-06.2006

Wallraff, A., Odermatt, B., Willecke, K., & Steinhäuser, C. (2004). Distinct types of astroglial cells in the hippocampus differ in gap

junction coupling. *Glia*, *48*(1), 36–43. https://doi.org/10.1002/glia.20040

Wilcock, D. M., Vitek, M. P., & Colton, C. A. (2009). Vascular amyloid alters astrocytic water and potassium channels in mouse models and humans with Alzheimer's disease. *Neuroscience*, *159*(3), 1055–1069. https://doi.org/10.1016/j.neuroscience.2009.01.023

Wu, Z., Guo, Z., Gearing, M., & Chen, G. (2014). Tonic inhibition in dentate gyrus impairs long-term potentiation and memory in an Alzheimer's disease model. *Nature Communications*, *5*, 1–12. https://doi.org/10.1038/ncomms5159

Yeh, C.-Y., Vadhwana, B., Verkhratsky, A., & Rodríguez, J. J. (2011). Early astrocytic atrophy in the entorhinal cortex of a triple transgenic animal model of Alzheimer's disease. *ASN Neuro*, *3*(5), 271–279. https://doi.org/10.1042/AN20110025

SUPPORTING INFORMATION

Additional supporting information may be found in the online version of the article at the publisher's website.